Characterization of Instrumentation and Assessment of the Quantitative Methods for the Full Kinetic Modeling of [^{11}C]CURB

by Charlotte F Labrie-Cleary

Master of Science Thesis

Department of Neuroscience, IPN

McGill University, Montreal QC

Submitted June 30, 2023

Table of Contents

i. Abstract (English)

The precise quantification of proteins in the brain using Positron Emission Tomography (PET) imaging requires additional instrumentation and rigorous validation of methodology. We can estimate sensitive indexes to quantify the protein of interest by measuring the concentration of radiotracer in arterial plasma (the input function) simultaneously to image acquisition and applying pharmacokinetic models. However, the metabolization of the PET radiotracers results in the formation of radioactive metabolites in the bloodstream. Therefore, the determination of the input function requires accounting for the contribution of the radio-metabolites in plasma, as well as the radioactive species in red blood cells (RBCs), platelets, and other blood components. In the present study, the instruments required for arterial blood sampling were characterized, as well as the assessment of the quantitative methods for the full kinetic modeling of [^{11}C]CURB, a radioligand that binds fatty acid amide hydrolase (FAAH) of the endocannabinoid system (eCB). More specifically: a) the performance of a fully programmable automatic blood sampling system (ABSS, Comecer®, Netherlands), used for the continuous measurement of arterial whole blood activity, was evaluated across a range of sampling conditions; b) The response of an automatic gamma counter (AMG, Hidex, Finland), used for measuring activity in samples of blood and plasma as well as determining the fraction of radiometabolites in plasma, was characterized for the range of expected experimental conditions; c) The sensitivity of different macroparameters derived from the kinetic modeling for detecting changes in [FAAH] with [^{11}C]CURB was studied; and d) the importance of the individualized details of the initial minutes of the arterial input function was assessed. This study provides a significant contribution in several aspects related to the precise and reproducible quantification of [FAAH] in the brain using [^{11}C]CURB PET imaging.

i. Abstrait (Français)

La quantification précise des protéines dans le cerveau à l'aide de l'imagerie par tomographie par émission de positons (TEP) nécessite une instrumentation supplémentaire et une validation rigoureuse de la méthodologie. En mesurant la concentration du radiotraceur dans le plasma artériel (la fonction d'entrée) simultanément à l'acquisition de l'image et en appliquant des modèles pharmacocinétiques, nous pouvons estimer des indices sensibles pour quantifier la protéine d'intérêt. Cependant, la métabolisation des radiotraceurs TEP entraîne la formation de métabolites radioactifs dans la circulation sanguine. Par conséquent, la détermination de la fonction d'entrée doit tenir compte de la contribution des métabolites radioactifs dans le plasma, ainsi que des espèces radioactives dans les globules rouges. Dans la présente étude, les instruments nécessaires à l'échantillonnage du sang artériel ont été caractérisés, ainsi que l'évaluation des méthodes quantitatives pour la modélisation cinétique complète du [^{11}C]CURB, un radioligand qui se lie à l'hydrolase des amides d'acides gras (FAAH) du système endocannabinoïde (eCB). Plus précisément: a) les performances d'un système automatique de prélèvement sanguin entièrement programmable (ABSS, Comecer®, Pays-Bas), utilisé pour la mesure en continu de l'activité du sang artériel total, ont été évaluées dans plusieurs conditions d'échantillonnage; b) la réponse d'un compteur gamma automatique (AMG, Hidex, Finlande), utilisé pour mesurer l'activité dans des échantillons de sang et de plasma ainsi que pour déterminer la fraction de radiométabolites dans le plasma, a été caractérisée pour la série de conditions expérimentales attendues; c) la sensibilité de différents macroparamètres dérivés de la modélisation cinétique pour détecter les changements dans la [FAAH] avec [^{11}C]CURB a été étudiée; et d) l'importance des détails individualisés des minutes initiales de la fonction d'entrée artérielle a été évaluée. Cette étude apporte une contribution significative sur plusieurs aspects

liés à la quantification précise et reproductible de la [FAAH] dans le cerveau à l'aide de l'imagerie TEP au [^{11}C]CURB.

ii. List of Tables

iii. List of Figures

iv. List of Abbreviations

eCB	Endocannabinoid System
CB1R/CB2R	Cannabinoid receptor type 1/type 2
AEA	N-arachidonoylethanolamine/anandamide
2-AG	2-arachidonoylglycerol
AA	Arachidonic acid
FAAH	Fatty acid amide hydrolase
PET	Positron emission tomography
[^{11}C]CURB	[^{11}C-carbonyl]6-hydroxy-[1,1′-biphenyl]-3-yl cyclohexyl carbamate (URB694)
Δ^9-THC	(-)-trans-Δ^9-tetrahydrocannabinol
SNP	Single nucleotide polymorphism
FOV	Field of view
sMRI	Structural Magnetic Resonance Imaging
PVE	Partial volume effect
CSF	Cerebral spinal fluid
RBC	Red blood cell
IF	Input Function
AIF	Automated arterial input function
APIF	Averaged peak input function
PBIF	Population-based input function
AUC	Area under the curve
PAP	Plasma-average peak

APWB	Average peak whole-blood function
SUV	Standard uptake value
IDIF	Image-derived input function
K*i*	transient receptor potential cation channel subfamily
B_{avail}	Enzyme receptor concentration
TCM	Tissue compartment model
TCM*i*	Irreversible tissue compartment model
rCBF	Regional cerebral blood flow
ABSS	Automatic blood sampling system
TAC	Time-activity curve
SPM	Statistical parametric mapping
SD	Standard deviation
PMT	Photomultiplier tube
MCA	Multi-channel analyzer
BBB	Blood-brain-barrier
HRRT	High-resolution research tomograph
PD	Proton density
ROI	Region of Interest
HV	Healthy Volunteer
CHR	Clinical high risk for psychosis
mCi	Millicurie
ABSS	Automatic Blood Sampling System
AMG	Automatic Gamma Counter

v. Acknowledgements

I would like to express my sincere gratitude to those who helped guide my success in completing my master's thesis. First, I would like to thank my supervisor Dr. Pablo M Rusjan for providing an intellectually stimulating environment to learn and for his mentorship, expertise, and guidance. Dr. Rusjan shared his expertise in PET neuroimaging and the compartmental modeling of radiotracers, and always encouraged me to push myself to be a better critical thinker and in turn a better researcher. I would also like to thank the members of my MSc supervisory committee: Dr. Corina Nagy, Dr. Pedro Rosa-Neto, and Dr. Sylvia Villenueve for their knowledge, support, and guidance.

This study would not have been able to be successful without the invaluable help of numerous researchers, radiochemists, and scientists at the Montreal Neurological Institute (MNI). I would like to thank the staff at the PET unit, Dr. Stephan Blinder and Arturo Aliaga, as well as the radiochemistry team at the MNI, including Dr. Gassan Massarweh, I-Huang Tsai, and Robert Hopewell, for providing us with quality samples for our characterization experiment and helping us with the initial setup of the radiometabolite laboratory. I would also like to thank Chris Hsiao, the PET technician, for his help in using and maintaining our gamma counting systems and for providing the necessary supplies for our experiments. I want to also thank our main collaborator, Dr. Romina Mizrahi, for her expertise in clinical research and for acting as a role model for a strong woman in STEM. Dr. Mizrahi's resilience and compassion for her work and patients is an inspiration and I am honored to have been able to work with her and her team.

Furthermore, I would thank my lab peers Ranjini Garani Ramesh, Kankana Nisha Aji, Christian Ramos, and Belen Belasco for their endless support, kindness, and guidance. Ranjini, thank you for taking the time to teach me everything there is to know about our lab's data and

analysis. Kankana, Christian, and Belen, thank you for showing me the ropes of clinical research and for your help in the radiometabolite lab. I would also like to say a special thank you to our Laboratory Coordinator, Manasi Oza, for her support and mentorship throughout my time at McGill, I could not have accomplished what I did without you.

Finally, I would like to emphasize my extraordinary thanks and gratitude to my family and friends, I would not be able to achieve my dreams without your support. I especially want to thank my mom, dad, and brothers for never letting me give up on myself and for their unconditional love.

Thank you all so much, you all played a pivotal role in my success!

vi. Contributions

Charlotte Labrie-Cleary (author): performed calibration experiments of instrumentation, developed standard operating procedures (SOPs), computed analysis and interpretation of data, and writing of the thesis document.

Dr. Pablo M. Rusjan (supervisor): conception and study design, guidance in study execution, provided mentorship throughout the study, results interpretation, and writing of the thesis document.

1. Introduction

1.1 Statement of Problem

Endogenous cannabinoids (endocannabinoids) are bioactive neurotransmitters that, when released by the post-synaptic terminal, activate their respective cannabinoid receptors CB1 and CB2 [1]. Endocannabinoids play a critical role in psychological parameters (e.g. motivation, learning, and stress responses) and have implications in psychiatric disorders (e.g. psychosis, depression, and anxiety) [1]. Fatty Acid Amide Hydrolase (FAAH) is the major metabolizing enzyme of endocannabinoid anandamide, known to modulate the signaling of CB1 and CB2 receptors [1]. Disturbances of FAAH activation and expression pathways have implications in various psychiatric behaviour and diseases [1]. Quantifying disturbances in FAAH concentration in the brain between healthy brain and neuroatypical brain could serve as a marker for disease pathogenesis [1].

[^{11}C]CURB was developed as a highly specific FAAH radiotracer used to explore the endocannabinoid system *in vivo* with positron emission tomography (PET) [2]. The quantification of [^{11}C]CURB binding in the brain via PET acquisition can be used as an index of FAAH concentration: the pharmacokinetic modeling of the PET time-activity curve defines the relationship between the measured data and the underlying biochemical parameters that influence the uptake and metabolism of the tracer [3]. The measured regional tracer distribution provides information about macro-scale physiological parameters in the tissue of interest that can be used to answer clinical and scientific inquiries about protein concentration. However, it is not possible without the study of the radioactive composition of arterial plasma due to the metabolization of parent compound post-bolus injection [4–6]. PET radiotracers are known to experience various chemical transformations once they enter the blood stream, which causes the

metabolization of the parent compound that break down into smaller component parts that can be easily excreted by the body [4, 7]. Arterial blood sampling is required for the accurate and reproducible construction of input curves defining the time course of blood radioactivity and tracer metabolization [4, 6]. There are many experimental and mathematical approaches available for the correction of tracer input functions for radiometabolite formation [4, 5, 8]. A common approach to radiometabolite correction uses a mixture of chromatographic procedures and mathematical modeling [3, 7–9]. The extraction and processing of arterial samples is considered a reliable method to construct reproducible results and representation of the delivery of radiotracer into tissue [28]. Arterial sampling requires catheterization of the radial artery for the extraction of whole blood radioactivity [28]. This method is however limited by its invasiveness and the necessity of additional instrumentation that require specially trained personnel and can be quite costly [6, 10, 11]. While the practice of using gamma counters and certain automatic blood systems are well established, the differences between hardware, conditions, and configurations across imaging facilities requires a careful design of customized operative procedures at each institution [12, 13].

1.2 Purpose

The goal of this project was to develop standardized operating protocols for the instrumental setup designed for the acquisition of reliable PET arterial blood data and to study its utility for the quantification of [^{11}C]CURB. The three specific aims within the goal of this thesis include (a) to setup and characterize the response of instrumentation needed for arterial blood sampling and radiometabolite blood composition in PET experiments, (b) to evaluate the impact of the temporally accurate measurement of blood radioactivity during the first 12 minutes of the quantification of the input function that is influenced by the rapid uptake and clearance of

[^{11}C]CURB from the blood stream following a bolus injection, and (c) to compare different parameters provided by the irreversible two-tissue compartment model used to quantify [^{11}C]CURB for the purposes of clinical experiments.

2. Background Information

2.1 Positron Emission Tomography (PET)

PET is a state-of-the-art technique for the non-invasive *in vivo* study of certain biochemical, physiological, and pharmacological functions of biomarkers at the molecular level [3, 14, 15]. PET imaging involves the decay of an unstable proton-rich nuclide emitting a positron (e^+) and a neutrino (ν_e),

$$p \rightarrow n + e^+ + \nu_e$$

Equation 1

where *p* represents the unstable proton and *n* is the resulting neutron [7, 16]. The annihilation of the positron with a nearby electron produces two collinear 511-keV gamma rays that travel in opposite directions and can be captured in coincidence by a multi-ring PET camera. The pair of activated detectors of the PET camera provide information for the special localization of the tracer concentration in the brain [7, 16].

The fundamental pipeline for PET imaging of the brain includes the administration of a radioactively labelled molecular probe into the peripheral bloodstream, to which its distribution and clearance in tissue is captured through the detection of the positron emitting isotope [16]. A suitable molecular probe should not disturb the underlying biological system under investigation; therefore probes are administered at tracer dose, which is determined by the lowest dose to achieve a high specific activity without exceeding 5% of the target receptor being occupied by the amount of tracer administered [7, 16]. Commonly used isotopes used for the labelling of molecular probes include ^{11}C, ^{13}N, ^{15}O, and ^{18}F which have relatively short half-lives that allows for repeat imaging by reducing the dose of radiation exposure to participants [7].

Brain PET imaging can be used as a powerful diagnostic and research tool to investigate disturbances in the biochemical processes that underlie brain disorders including neurodegenerative disease, addiction, cancer, and mental illness [9, 15].

2.2 Principles of PET Imaging in the Human Brain

Reconstruction algorithms convert the photons counted by the cylindrical arrangement of detectors in the PET scanner in to static (3D) or dynamical (4D) images [17, 18]. Reconstruction algorithms can be used to perform appropriate corrections to account for scatter and attenuation [3]. The photons created from the annihilation of the emitted positron must pass through tissue (skull/head) before reaching the PET detector, and this photon-tissue interaction in the field of view (FOV) leads to photon attenuation [18]. Photon attenuation can cause upwards of 90% signal reduction in some regions of interest (ROI), therefore an attenuation correction is essential to quantitative PET imaging practices [18]. The effect of attenuation on the PET signal can be described by a mono-exponential function,

$$\frac{I}{I_0} = e^{-\mu L}$$

Equation 2

where I is the non-attenuated and I_0 is the attenuated PET signals, and the variables of the exponential function, μ and L, represent the linear attenuation coefficient (LAC) and thickness of a tissue [18]. A common technique for correcting for scatter and attenuation in dynamic PET imaging is the estimation of attenuation maps through a transmission scan using a gamma emitting radionuclide source with a long half-life, such as ^{68}Ge/^{68}Ga or ^{137}Cs [18].

The spatial and temporal resolution of the PET scan is limited due to several factors, such as the detector size, noncollinearity (the larger the detector ring the lower the spatial resolution), and head motion [7, 17]. As a result, PET quantification can be improved with additional

imaging modalities. The most common approach is the use of structural Magnetic Resonance Imaging (MRI). A MRI must be acquired for each subject undergoing PET scanning to help with the delineation of the anatomical structure and partial volume effect (PVE) correction [17]. This multi-modal method requires additional mathematical segmentation algorithms to co-register the MR and PET images through the segmentation of gray matter, white matter, and cerebral spinal fluid (CSF) to define distinct ROIs [18, 19].

The time course of the radioligand in a given ROI depends on the physical characteristics of the tissue of interest (e.g. concentration of the target) as well as the Input Function (IF) [3]. The IF represents the time course of the net availability of radiotracer in arterial plasma. It is mathematically constructed from the data acquired during the continuous measurement of whole blood radioactivity and corrected for red blood cells (RBCs), other blood component contribution, and for radiometabolite concentration [3]. A common analytical technique for acquiring whole blood radioactivity during PET acquisition is by radial arterial sampling [2, 3, 5]. An automatic blood sampling system (ABSS) can be used to continuously measure the concentration of activity in arterial whole blood [10]. While this is an efficient way to measure whole blood activity, it is necessary to extract additional manual arterial samples to determine the concentration of radioactivity in plasma and the fraction of that activity due to the unmetabolized radioligand [2].

In brain studies, PET imaging can be used to measure regional brain radioactivity, which comprises of the sum of brain tissue and blood volume contributions [3, 14]. Although, to understand the underlying biochemical parameters that influence the uptake and metabolism of the tracer, mathematical tracer kinetic modeling is required [3]. There are several constraints and assumptions on the nature of radioligand binding that must be met in order for a model to

accurately represent what is happening on a physiological level [3, 14]. For this reason, it is essential to validate the parameter(s) of interest provided by the kinetic model with experimental challenges (e.g. pharmacological inhibition of the target) and reproducibility studies (e.g. test-retest paradigms) [3]. The outcome of a kinetic model is a parameter, usually as a composition of rate constants, which under ideal model conditions, are proportional to the concentration of the physiological target under investigation [7].

2.3 Kinetic modelling

The result from dynamical PET imaging produces a regional Time-Activity Curve (TAC) in distinct ROIs in the brain. The TAC is a temporal measure of the radiotracer concentration in the tissue of interest [7]. Mathematical compartmental models help to improve the type and quality of information that defines the relationship between the measurable data and biological parameters that affect the TAC [3]. The accuracy of the quantification using compartmental modeling is heavily influenced by the accuracy of the reconstruction algorithm and the level of noise [3]. The level of noise present in a given compartmental model is influenced by several factors such as the injected dose, camera sensitivity reconstruction parameters, scan length, and the size of the ROI [3]. The amount of noise in the TAC will determine the quantity and precision of extracted parameters [3]. The number of compartments that are considered in a given model will determine the quantity of variables of the model (usually representing the rate constants) [3]. A general PET compartmental system (Figure 1) consists of the total radioactivity in tissue concentration (C_T), the parent concentration (C_P), and the whole blood concentration (C_B) [20]. The rate at which the radiotracer will undergo certain biochemical transformations as it moves from one compartment to another follows first-order kinetics, characterized by a rate constant k, and can be predicted by implementing a refined mathematical model that is

developed based on the expected *in vivo* behavior of the radiotracer [3, 21]. All constants are in units of inverse time (min^{-1}) with the exception of the rate constant K_1, which is capitalized to denote different units of measure as it represents the volume of blood (or arterial plasma) per volume of tissue per minute ($mL \times mL^{-1} \times min^{-1}$) [22]. The term microparameter is used here to distinguish the global system parameters that are a function of the individual rate constants, which have shown to be more stable with respect to parameter estimations [14].

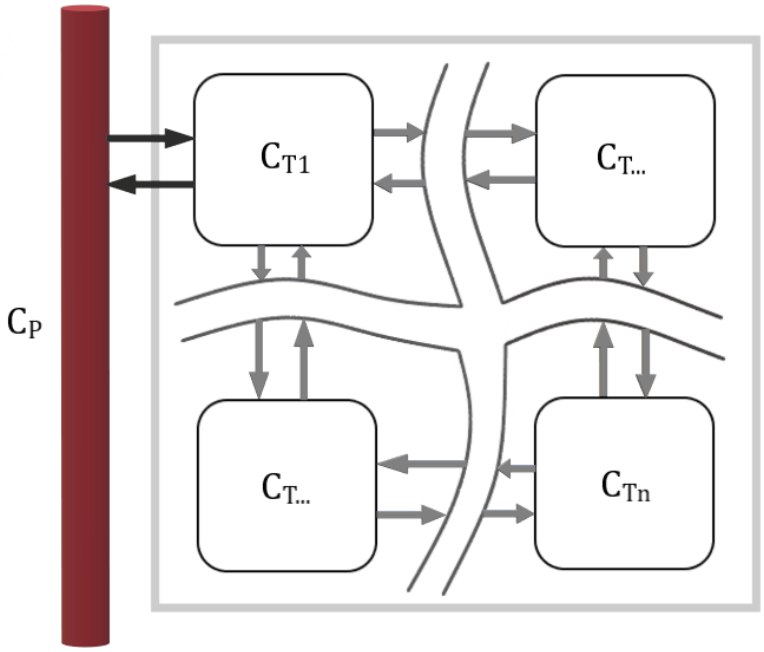

Figure 1. General tissue compartmental model.

Compartmental models uses relatively simple algorithms to define the physical location, state, and potential transformations of radiotracer from one compartment to another [3]. For these relatively simple compartmental models to successfully represent the complex biological system under investigation, several assumptions must be met and validated to produce acceptable levels of errors in parameter estimation [3]. The two major assumptions in compartmental modeling are (1) each compartment is homogenous and is null of any concentration gradient within a single compartment, meaning that all radiotracer molecules in a given compartment have equal probability of exchange into other compartments without being driven by external

biochemical forces, and (2) the underlying physiological processes are in steady-state, meaning that the rate constants are actually constant throughout the time-course of the PET study [3]. In clinical practice, generally it is impossible for all assumptions of a given model to be met, but as long as they produce an acceptable level of error in the computation, the model should be successful in estimating parameters [3].

2.4 PET Imaging of FAAH in the Brain with [^{11}C]CURB

[^{11}C-carbonyl] 6-hydroxy-[1,10-biphenyl]-3-ylcyclohexyl carbamate ([^{11}C]CURB) is a novel radiotracer for quantifying FAAH in the human brain [23]. The radiotracer was generated from the analog of the FAAH inhibitor URB597, 6-hydroxy-[1,10-biphenyl]-3-ylcyclohexylcarbamate (URB694) using the [^{11}C]CO_2 fixation technique, yielding [^{11}C-carbonyl]URB694, otherwise known as [^{11}C]CURB [2]. [^{11}C]CURB makes strong covalent bonds by carbamylating the active site of FAAH, and is therefore irreversibly bound [2, 25, 26].

2.4.1 The Endocannabinoid System (eCB)

During the intricate transmission of information by chemical signals, neurotransmitters serve as the fundamental mode behind intercellular communication in the central nervous system [26]. In recent years, lipids have emerged as an interesting and important classification of chemical messengers in the nervous system, operating through distinct mechanisms that differ to the classic model for neurotransmission [26]. The synthesis of lipid transmitters is activated on-demand, wherein the biosynthesis and subsequent release by neurons occurs at the exact moment of their intended operation [26]. Lipid signalling is heavily regulated by the action of metabolic degrative enzymes that will ultimately determine the strength and duration of activation [26]. The eCB is one of the most prominent lipid transmission regulatory system in the brain that heavily impacts neuronal synaptic communication responsible for several biological and

psychological functions including, eating, learning and memory, depression, anxiety, reproduction, growth and development, and metabolism [1, 27].

2.4.2 Endogenous Cannabinoid Signaling and Degradation

Endogenous cannabinoids (endocannabinoids) are a class small molecules that activate G-protein coupled cannabinoid receptors CB1 and CB2, the same receptors that have biochemical specificity for the psychoactive component in cannabis, (-)-trans-Δ^9-tetrahydrocannabinol (Δ^9-THC) [26]. CB1 receptors (CB1R) are primarily expressed in the CNS by neuronal cells, and some non-neuronal glial brain cells including oligodendrocytes, microglia, and astrocytes. CB1Rs are responsible for modulating neurotransmission release through retrograde inhibition at the pre-synaptic terminal [1]. CB2 receptors (CB2R) are mainly expressed in the peripheral nervous system by immune cells (e.g. B-cells and natural killer cells), microglia, and to a lesser degree, in neurons localized in the brainstem [1, 28–30]. In the eCB, the two primary endocannabinoids that activate CB1R and CB2R that have been identified in mammals are *N*-arachidonoyl ethanolamine (anandamide) and 2-arachidonoylglycerol (2-AG), which act as retrograde messengers [26].

2.4.3 Fatty Acid Amide Hydrolase (FAAH) in the eCB

FAAH is the major terminating and degradation enzyme of endocannabinoid anandamide, known to modulate the signaling of CB1 and CB2 receptors associated with psychiatric disorders [1]. FAAH is an integral membrane protein, heavily expressed in the nervous system, that possess multiple activation domains for receptor membrane association [26]. FAAH is a part a class of serine hydrolases composed of a catalytic triad of residues: Lys142-Ser217-Ser241, with Ser241 acting as the catalytic nucleophile [31]. The inhibition of

FAAH is known to be associated with effects that mirror those found in cannabinoid signaling including analgesia, hypomobility, hypothermia [32].

2.4.4 FAAH in Clinical Research

In the eCB, anandamide and 2-AG are synthesized on-demand in the nervous system, and their specificity includes CB1Rs that play a pivotal role in neurotransmitter release [1, 26]. Anandamide and 2-AG are regulated by specific biosynthetic and degradative pathways, and their synthesis and subsequent degradation is a highly regulated process [26, 27]. During anandamide degradation, it will undergo chemical hydrolysis to form arachidonic acid (AA), primarily by FAAH at the level of the postsynaptic neuron [1, 33]. FAAH has shown to play a major role in a wide range of neurophysiological processes, including nociceptive pain mechanisms, neuroinflammation, anxiety, and depression [26, 27]. Disturbances of FAAH activation and expression pathways have implications in various psychiatric and mood disorders [1]. The *in vivo* mapping of FAAH in the brain by PET is a useful approach to investigate alterations in the eCB [34, 35].

2.4.5 Kinetic modeling of [^{11}C]CURB

The distribution and nature of [^{11}C]CURB binding was evaluated to develop quantification procedures for measuring FAAH in the human brain using PET. [^{11}C]CURB compartmental modeling was first assessed using PET imaging of six healthy control participants (3 M, 3 F) [2]. It was found that an irreversible two-tissue compartmental model (denoted here as 2-TCM*i*) better fit the 60 min TACs than other compartmental models, such as the two-tissue compartmental model (2-TCM). The identifiability of various parameters provided by the 2-TCM*i* to index FAAH activity in the brain were assessed.

The 2-TCM*i*, depicted in Fig. 1, uses compartments to represent biochemical states of [^{11}C]CURB as it crosses the blood-brain-barrier (BBB) from the plasma compartment (C_P) into tissue (C_T). In Fig 2, K_1 represents the rate constant of transfer of [^{11}C]CURB from plasma into the free and non-specifically bound compartment (C_{F+NS}), k_2 is the rate constant for the efflux of radioligand from the C_{F+NS} back into C_P, and k_3 is the rate constant for the transformation of radioligand from the C_{F+NS} to the specifically bound irreversible compartment (C_S) [3, 22, 24]. Defining F as the perfusion or blood flow, PS as the permeability surface area product, and E is the first pass extraction factor: $E = 1 - e^{\frac{PS}{F}}$, using the Renkin–Crone model [2, 36]:

$$K_1 = FE$$

Equation 3

And defining Lambda ($\lambda = K_1/k_2$) as the distribution volume of the ligand in the C_{F+NS},

$$k_2 = K_1/\lambda$$

Equation 4

Under the assumption that the radioligand is administered at tracer dose and the available density of target (B_{avail}) does not change along the PET experiment, k_3 can be related to B_{avail} using:

$$k_3 = f_{ND} k_{on} B_{avail}$$

Equation 5

where f_{ND} defines the non-displaceable fraction of tracer that is freely constituted in tissue and k_{on} represents the [^{11}C]CURB-FAAH association rate constant, [2, 22].

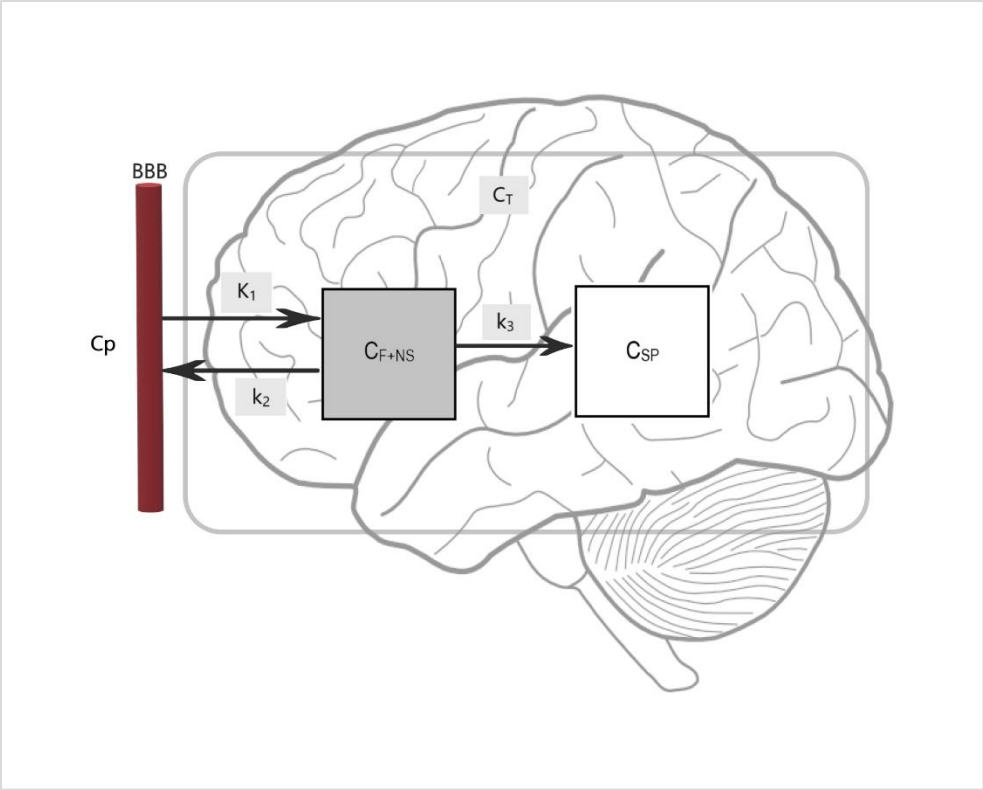

Figure 2. The structure for the irreversible two-tissue compartment model (2-TCM*i*) and its macroparameters. From this model two parameters are computed to quantify the nature of specific binding of radiotracer in the tissue compartment (C_T) which is proportional to the concentration of target in the brain.

K_i represents the unidirectional uptake rate constant, as it incorporates both net inward transport and trapping of the radiotracer in tissue [37]. This parameter is defined by the product of the terms K_1 and $k_3/(k_2 + k_3)$, the fraction of the tracer that reaches the specifically bound irreversible compartment (C_S) in the tissue:

$$K_i = \frac{K_1 k_3}{k_2 + k_3}$$

Equation 6

The results reported by Pablo Rusjan *et al.* (2013) support λk_3 as an optimal index of FAAH due to its sensitivity to changes, cancellation of correlation between rate constants and independence of cerebral blood flow [2].

Blocking experiments of the FAAH enzyme in humans using a highly specific urea-based FAAH inhibitor (Pfizer Inc., NY), PF-04457845, were conducted to confirm the validity of the

2-TCM*i* [38]. The TACs of [^{11}C]CURB showed a dramatic change in respect to the baseline in a second scan following the administration of PF-04457845. It was observed that no further changes in the [^{11}C]CURB TACs appeared with the increasing single-doses higher than 1 mg, allowing the unequivocal characterization of the free and nonspecific binding of the radioligand [38]. The results from this study provided strong evidence for the validation of the use of λk_3 computed using a 2-TCM*i* to quantify FAAH activity in the human brain [38].

The evidence provided also demonstrated that K_i, and k_3 have excellent identifiability and convergence for all ROIs at 60 and 90 minutes [2]. Depending on the ratio k_2/k_3 the quantification of a radiotracer that irreversibly binds to its target could be compromised by the cerebral blood flow [2]. When $k_3 >> k_2$, all the concentration of radioligand that crosses the BBB is immediately bound to the target, and the radioligand uptake is more sensitive to changes in regional cerebral blood flow (rCBF) than changes in the concentration of target. As [^{11}C]CURB is an irreversible radiotracer, the kinetic parameters could be susceptible to varying rCBF [2]. Moreover, the net influx K_i, is a function of cerebral blood flow through K_1 and k_2. It is preferable to express [^{11}C]CURB binding in terms of the composite rate constant, λk_3, since it is independent of the influence of rCBF [2, 39]. λk_3 helps eliminate the effect of rCBF when quantifying irreversible radioligands, because it contains the ratio K_1/k_2, and helps minimize the effect of the correlation between the parameters k_3 and k_2 [2]. Furthermore, λk_3 is directly proportional to k_3, and thus more sensitive to changes in specific binding than K_i which presents a non-linear dependence on k_3 [2].

2.5 Determining the Arterial Input Function

2.5.1 Radiometabolites

Immediately following intravenous administration, PET radiotracers are exposed to complex chemical environments in the blood stream that include various metabolizing enzymes that break down the parent radiotracer into one or more metabolites [5, 40]. During radiotracer metabolization, a portion of the radioactive isotope tags are transferred to the forming radiometabolites [4, 41]. The signal detected by the PET in the FOV captures all positron emitting signals and represents the total amount of radioactivity, but it is unable to distinguish whether the signal originates from the parent compound or its radiometabolites [4, 41]. In a "good" radioligand, radiometabolites are more polar than the parent radioligand, and therefore it is expected they are unable to cross the BBB. Therefore, the activity inside of the tissue is expected to come only from the parent compound.

2.5.2 The Gold Standard – Arterial Input Function

The standard method for determining the arterial input function is through the continuous measurement of blood radioactivity simultaneously to the PET scan acquisition [5, 42]. It can be done by rapid manual sampling, integrated automated handling systems, or through the use of automatic sampling devices [10, 43]. Performing manual sampling for the determination of the arterial IF is disadvantageous due the limitation of the time resolution at which the samples can physically be acquired, which can introduce higher levels of uncertainty into the data analysis [10]. Therefore, due to the high workload and resources required for manual sampling to determine the arterial input function, it is generally preferable to acquire continuous blood activity measurements using an automated sampling system in combination with manual sampling for the correction of radioactivity coming from RBC, platelets, white blood cells and

radiometabolites [10, 43, 44]. Alternative methods for the simplification of determining the arterial IF have been proposed and are used by some research groups, including arterialized-venous sampling, population-based IF (PBIF), image-derived IF (IDIF). When a region devoid of specific binding exists (reference tissue) binding parameters can be determined without the IF [42].

2.5.3 Venous Sampling

Venous sampling can be used as an alternative to arterial blood sampling by applying heat to the limb, from which the samples are withdrawn, to about 44°C, termed by many as the arterialization of venous blood [42]. The heating of the limb causes vascular dilation and increases the venous blood flow, therefore the venous blood starts to become indistinguishable from arterial blood [42]. The accuracy of venous sampling method for determining the input function curve is, however, limited by some factors including inconsistent concentrations of radioligand over time [45–48]. The concentration of tracer in the veins takes longer to reach equilibrium, and this time frame varies between radiotracer [49]. As a result, the arterial tracer kinetics vary significantly to that of venous [48, 49]. While arterialized-venous sampling can help the venous concentrations to be more consistent to that of arterial concentrations, it is still limited by the effect of delay and dispersion, and the uncertainty of measurements within and across subjects that introduces higher levels of uncertainty into the TACs [45–47, 50, 51].

2.5.4 Population-Based Input Function (PBIF)

PBIF scales an average input function created from the IF of a population of subjects previously scanned [44]. The scaled PBIF is then used for the kinetic modelling of imaging data for individual subjects [44, 52]. The averaging of the individual input functions entails shifting the individual curves to align the peaks, which are then normalized using the injected dose, and

body mass [44]. Typically PBIF quantification can be successfully applied if the nature of tracer biodistribution and metabolization that define the shape of individual IFs behave similarly to the population average IF, and ideally should only differ in magnitude [53]. Generally, to accurately scale the PBIF for each subject requires at least one or more manual arterial samples to obtain concordance to that of the AIF [44, 54, 55]. It is possible to accomplish successful estimations without the use of blood sampling, but the correlation to the original plasma input is strong and the variation will be smaller in metabolite corrected PBIFs [44, 54]. However, using the PBIF method has limited identifiability and is usually less sensitive at detecting subtle group differences at an individual level and therefore should be used with caution [54]. PBIF should not be used when the IF can be influenced by the condition that are being studied such as disease or pharmaceutical interventions.

2.5.5 Image-Derived Input Function (IDIF)

IDIF calculates an estimate of the arterial IF curve directly from the PET images to represent the tracer activity in blood, which eliminates the need for invasive arterial cannulation, blood analysis, and specialized personnel, for some radioligands [44, 49]. An IDIF generated input function curve is generated using the vasculature as the ROI, and in the case of brain PET imaging the carotid arteries are typically used [44]. The accuracy of using IDIF is dependent on several factors including the intrinsic spatial resolution of the PET scanner, the type of reconstruction algorithm implemented, as well as the definition of the ROIs [44]. IDIF methods for estimating the input function is a desirable alternative to arterial sampling, although there are several methodological challenges that limit the prevalence of IDIF in brain PET imaging [49, 56]. IDIF methods are limited primarily by the spatial resolution and the resulting PVE, which causes quantitative underestimation of the activity concentrations in the reconstruction of the

images and therefore the underestimation of the input function curve [49, 57]. Using IDIF methods that do not require blood sampling relies on the number of voxels to estimate the blood activity, but the accuracy of these methods have shown to be unpredictable, and therefore using blood-sampling based IDIF methods have proven to be more reliable [56]. In general, the use of IDIF to calculate the input function can be used as an adequate simplification, but the success of its implementation can be challenging [49]. Several factors must be considered to accurately implement IDIF methodology, including the careful evaluation and validation the specific tracer of interest, the difficulty of obtaining accurate estimations of metabolite formation from the image input alone, and the method for PVE corrections [56, 57]. The IDIF-method has been studied primarily using the radiotracer [^{18}F]FDG [58], which can provide accurate results using a method validated by Chen *et al.* (1998). However, for most radioligands the effect of tracer metabolization is a major concern and requires the quantification of parent compound in plasma. Using an estimate of the whole-blood curve will be insufficient to estimate accurate measures of the input function and neglects the influence of radiometabolites, and therefore using IDIF-methods is not practical for most PET tracers [49]. In practice, to use IDIF-methods for the input function, it requires significant efforts put towards the validation and requires at least some arterial blood sampling for the adequate identifiability and to improve the parameter estimations [49].

2.5.6 Reference Tissue Models

A reference tissue (R_{ref}) model relies on a region in the brain that fits the following criteria: (1) it is devoid of any specific binding of the radioligand being used, (2) the uptake of the radioligand is not affected by disease process or treatment, and (3) the non-specific binding of tracer is similar to other ROIs [44, 59, 60]. The use of a R_{ref} compartmental model eliminates

the need for invasive arterial blood sampling and the need for the plasma input function, and instead uses measures from the TACs of the reference region [59–61]. Typically, R_{ref} models use the estimates of the binding potential (BP_{ND}) from reversible radioligands, which describes the ratio of the total density concentration of receptors (B_{max}) to that of the equilibrium dissociation constant (K_D) [22, 62]. By comparing the kinetics of the radioligand in the target ROI with that in the R_{ref}, it is possible to estimate the BP_{ND}. One commonly used reference region model is the Simplified Reference Tissue Model (SRTM), initially proposed by Lammertsma and Hume (1996). In the SRTM, assumption is that the BP in the reference region is negligible, and the ratio of the radioligand concentration of the target and reference regions at equilibrium is equal to the ratio of the binding potentials in the target and reference regions [59]. This model provides a simplified way to estimate BP without the need for explicit knowledge of the arterial input function [59]. Another widely used reference region model is the Logan Plot, using a graphical analysis of the PET data, in which the distribution volume ratio (DVR) is an index for estimations of B_{vail} without the need of blood sampling [63]. Both SRTM and the Logan Plot have been extensively applied in PET imaging of various molecular targets in the brain, however, it is important to note that the choice of an appropriate reference region model depends on the specific radioligand and target of interest, as well as the characteristics of the reference region itself [59, 63].

2.6 Arterial Blood Sampling in PET Imaging

While several approaches for estimating the plasma input function are available, the gold standard approach remains arterial blood sampling for each subject. Nevertheless, there is a demand for employing less intrusive and increasingly automated techniques in image analysis to

enhance the engagement of study participants and improve the dependability of analysis methods.

The quantification of [^{11}C]CURB requires the correction for radiometabolite formation in the plasma input function curve for the accurate full kinetic modeling of radioligand in tissue [42]. There are some possible complications with arterial cannulation, including bleeding, occlusion, infection, and blood clotting [6]. Nevertheless, arterial sampling has demonstrated to be a safe and reliable methodology for PET clinical studies [6]. Considering the minimal risk to participants, arterial sampling is used for the quantification of FAAH in the brain using [^{11}C]CURB imaging, as it represents the true delivery function of parent radiotracer in arterial plasma [6].

2.6.1 Plasma Metabolite Analysis

Due to their lipophobicity, the radiometabolites formed during [^{11}C]CURB PET imaging are confined to the periphery and are unlikely to cross the lipid bilayer of the BBB to enter into the brain [23]. However, in the blood, there are contributions of radiolabeled species in the plasma, RBC, and other blood components. In consequence, the concentration of radioactivity in plasma must be corrected for the radiometabolite contribution before being used as the input for modeling the tissue kinetics [5]. There are several approaches to measuring the fraction of unchanged radioligand in plasma (the Plasma Parent Fraction or PPf) for quantitative dynamic PET imaging [5]. The most commonly used methods of PPf measurement include high-performance liquid-chromatography (HPLC), thin-layer chromatography (TLC), and other chromatographic methods such as solid-phase extraction (SPE) and column chromatography [5, 8].

SPE using a universal sorbent for acidic, neutral, and basic compounds equipped with a ratio of two monomers, the hydrophilic N-vinylpyrrolidone and the lipophilic divinylbenzene, has previously been validated for the extraction of radiometabolites from parent compound for [^{11}C]CURB imaging studies [2, 23]. To ascertain the contribution of radiometabolites to the plasma input function, individual manual samples at various time points during the scan are processed using Oasis® HLB filter apparatuses, which are hydrophilic-lipophilic-balanced, water-wettable, reversed-phase SPE sorbent cartridges. The radioactivity of the parent compound trapped in the Oasis® filters is measured, and this data is later used to account for percent metabolization in the plasma input function calculations.

2.6.2 Automatic Blood Sampling System (ABSS)

The continuous measurement of the early arterial blood radioactivity was counted using the Programmable Blood Sampler (PBS-101, Comecer, The Netherlands). The PBS-101 ABSS is a fully programmable system developed specifically for the continuous measurement of arterial radioactivity concentration for quantitative PET analysis [11]. The ABSS is equipped for the detection of 511-keV annihilation photons using a 6-cm-diameter bismuth germanate (BGO) crystal, coupled with a photomultiplier tube (PMT), and a multichannel analyzer (MCA) [10, 11]. Using this system, a patient's arterial blood is withdrawn using 1-mm low-retention tubing at a flow rate regulated by a peristaltic pump [10, 11]. The detector system is protected by 6-cm lead shielding, with a 3-mm slit for positioning the tubing for the continuous measurement of blood [10]. The acquisition length and pump-rate intervals are all controlled remotely by an external PC with an established RS-232 connection to the pump, detector, PMT, and MCA [10]. The spectral data is acquired and sorted into two ROIs that are manually predefined during system calibration [10, 11]. For clinical purposes, it is necessary to perform routine calibration

and quality control to ensure reproducibility and accuracy during operation of the ABSS. The regions of interest are delineated using a gamma-emitting needle source (Germanium-68, Sanders (Med/Cal), PET-168/3.8, Serial No. K156-K158) to obtain total counts for both the 511-keV and 1022-keV energy windows [10, 11].

Additional procedures are performed to cross-calibrate and to synchronize the internal clock of the ABSS to the other devices in the institution, including the Capintec™ Dose Calibrator, the PET scanner, and the automated gamma counter.

2.6.3 Hidex NaI Automatic Gamma Counter (AMG)

During [^{11}C]CURB dynamic PET imaging, the continuous arterial sampling of radioactivity is supplemented with several manual arterial samples at various time points. Those samples are used to convert the concentration of radioactivity in blood into the plasma input function. It involves (1) a correction for radioactivity in RBC and other blood components, and (2) a correction for radiometabolite in plasma [24, 42]. The concentration of radioactivity of each sample of blood and plasma is measured using a high-performance automatic gamma counter (Hidex Automatic Gamma Counter (AMG), Hidex, Finland) with a 3-inch NaI crystal detector and 55-mm lead shielding. The AMG is equipped with a linear multichannel analyzer for powerful spectrum analysis, consisting of a total of 2,048 channels and an energy range of 15-2000 keV. The AMG is equipped with a total of 12 racks holding 6 vials of up to 28-mm diameter, or 22 racks holding 10 vials up to 13-mm in diameter. Once loaded, the samples are individually removed from the rack by a robotic operator to be weighed and placed in the well of the crystal detector for measurement.

Like the PBS-101 ABSS, the Hidex AMG requires cross-calibration and synchronization of the internal clock with the other devices in the institution such as the HRRT PET scanner. Cross-calibration should consider the effect of sample volume and geometry (including height, width, and length of tubing used) on the efficiency for the specific radioisotope under evaluation [64]. The practice of using NaI crystal gamma counters is well established, although standardization across imaging facilities is poorly defined [12, 13]. There are several factors that contribute to the efficiency of a gamma counter, including sample geometry (Fig. 3), the effectiveness of shielding, and calibration accuracy [12].

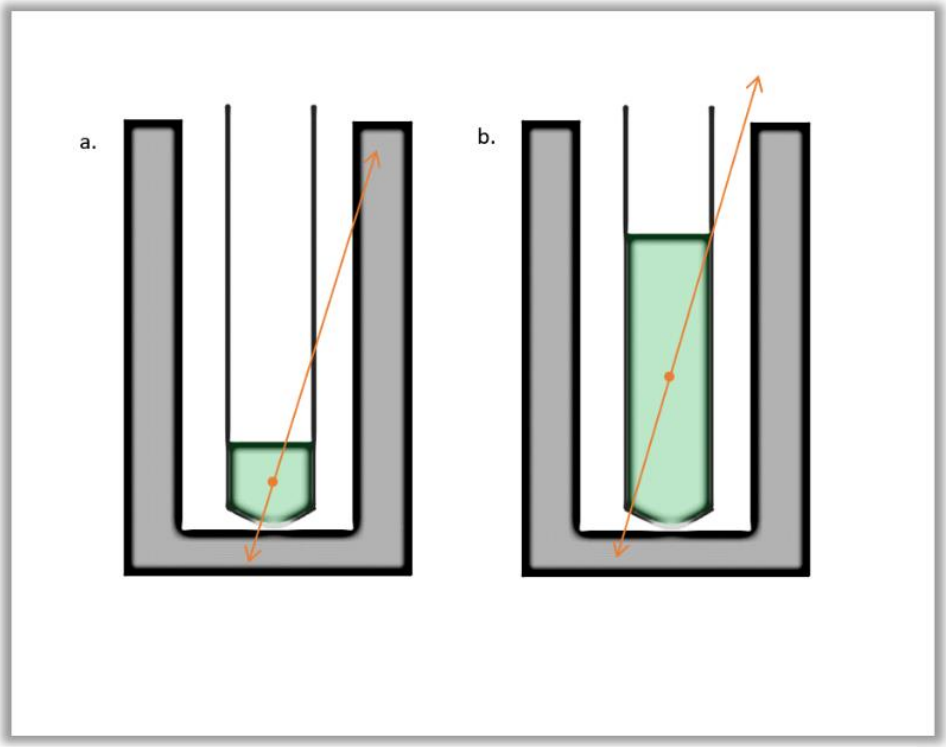

Figure 3. Effect of sample volume on capture of photon emission in crystal detector. (a) Orange arrows provide an example of a pair of annihilation photons that contribute to coincidence sum peak in NaI well. (b) Demonstrated the increasing likelihood of the escape of photons from the top of the well as sample volume increases [12].

2.7 Rationale, Aims, and Hypotheses

2.7.1 Aim I: Characterization of Instrumentation

The quantitative requirements for clinical in-vivo PET studies necessitates rigorous cross-calibration and time synchronization between instrumentation to minimize error factors, determine optimal isotope-specific operational range, and maximize accuracy of measurements [12].

a. ABSS Calibration and Delineation of ROIs

Before using the PBS-101 for data acquisition and the creation of the IF, it is necessary to experimentally find the cross-calibration factor necessary to integrate the instrument to the other devices in the PET center. Individual calibration is required for every imaging facility and environment in which the ABSS is used. Therefore, the goal of this objective was to determine the count efficiency, reproducibility, and effect background radiation of the radioactivity measurements acquired by the PBS-101 ABSS at the MNI under different experimental conditions.

b. Response of the Hidex NaI AMG

The reproducibility and performance of NaI gamma counters have an important role in clinical applications, including *in vivo* PET neuroimaging [12, 65]. The characterization of external influences on the gamma counts of the AMG must be experimentally determined to correct measurements for background noise and sample volume effects (Fig. 3), and to quantify the count efficiency of individual measurements for different radionuclides [12].

The goal of this work was to characterize the response and determine the efficiency and optimal counting range of activity for the isotopes ^{11}C and ^{18}F, with varying concentration and sample volumes.

Hypothesis: The response of the AMG would be stable with minimal uncertainty and the calibration of the γ-counting efficiency will be stable and identifiable with respect to the dose calibrator.

2.7.2 Aim II: Investigation into the Identifiability and Sensitivity between [^{11}C]CURB Macroparameters

Is has been shown that a functional single-nucleotide polymorphism (SNP) in human the FAAH gene of the eCB that involves the transversion of the nucleotide cytosine to an adenine (rs324420, C385A) that results in lower FAAH levels in the brain [66, 67]. The prevalence of FAAH variants are 58% C/C, 28% A/C, and 4% A/A. [^{11}C]CURB binding to FAAH was able to detect this difference. Using λk_3 as an index, A-allele carriers had a 23% lower level of FAAH expression [66]. While it was previously demonstrated that the parameters K_i, k_3, and λk_3 presented as acceptable parameters to quantify FAAH binding [2], their identifiability and sensitivity to detect changes in brain FAAH vary.

The goal of this study was to compare the sensitivity of three macroparameters of [^{11}C]CURB 2-TCM*i*: K_i, k_3, and λk_3. The power of each parameter to predict the observable polymorphism effect between the C/C and A/C SNPs in the rs324420 FAAH gene was investigated to assess the most effective method for FAAH quantification using [^{11}C]CURB.

Hypothesis 1: The macroparameter, λk_3, will have the highest sensitivity for detecting changes in FAAH binding between C/C and A/C rs324420 SNPs in smaller ROIs.

Hypothesis 2: k_3 will have the highest sensitivity for detecting changes FAAH binding in large ROIs.

2.7.3 Aim III: Average Peak Arterial Input Function (APIF)

The accurate quantification of [^{11}C]CURB binding to FAAH requires arterial blood sampling. As described before we use an ABSS to sample at high frequency the peak of the activity in blood following the bolus injection. While the main drawback of arterial blood sampling is the arterial cannulation, ABSS operation has their own challenges which often produces the loss of the data. The arterial cannulation procedure may cause moderate to severe discomfort to the participant and discourage them from participating in the study as a result. In addition, a major obstacle that can arise during arterial blood samples experimentation is the clotting of blood in the tubing, causing partial or complete blockages that impedes data collection [10, 54]. The ABSS suffers some other artifacts influence the quantitative accuracy of arterial sampling, including the dispersion, delay, and affinity to tube lining during blood withdrawal [5, 68].

The goal here was to develop a computational approach to overcome the potential complications associated with the use of the ABSS to calculate an individual automatic input function (AIF) and to understand the amount of detail required in the initial high frequency sampling immediately after bolus injection to produce robust outcomes. The present study evaluated the bias and variability introduced to [^{11}C]CURB λk_3 when implementing an averaged peak input function (APIF) for its kinetic analyses. The main purpose of this study was to establish a standard protocol for recovery of lost data due to a ABSS failure during data collection. We also evaluated the importance of individual ABSS measurements for [^{11}C]CURB PET imaging.

Hypothesis: The macroparameter, λk_3, computed using the APIF will be sufficient in reproducing the SNP rs324420 polymorphism effect of [^{11}C]CURB binding to FAAH.

3. AIM I: Characterization of Instrumentation for Arterial Sampling of [^{11}C]CURB

3.1 Methods

3.1.1 Objective A: ABSS Calibration and Delineation of ROIs

The energy spectrum of the PBS-101 ABSS was calibrated using a ^{68}Ge (Sanders (Med/Cal) Rod Sources for PET, PET-168/3.8, $t_{1/2}$ = 270.95 days, Eγ = 511/1022 keV) needle-point source inserted into the MCA detector. After a 160 second acquisition, the peak of 511 keVs in the spectrum was used to adjust the high tension setting of the ABSS to match the channel corresponding to 511-keV. Later the channels corresponding to the peaks of 511 and 1022-keV energy peaks were used to determine two energy windows "ROIs" for counting during the blood acquisition. The ROIs comprise the channels 238-438 and 576-776. The process with the ^{68}Ge needle-point source is repeated before the beginning of each PET scan to ensure that the spectrum peaks remain in the center of each ROI counting window. The cross-calibration factors to both the AMG and PET scanner under different experimental conditions, including shutting

the ABSS on/off, moving the position of the arterial catheter, and changing the count time, were computed.

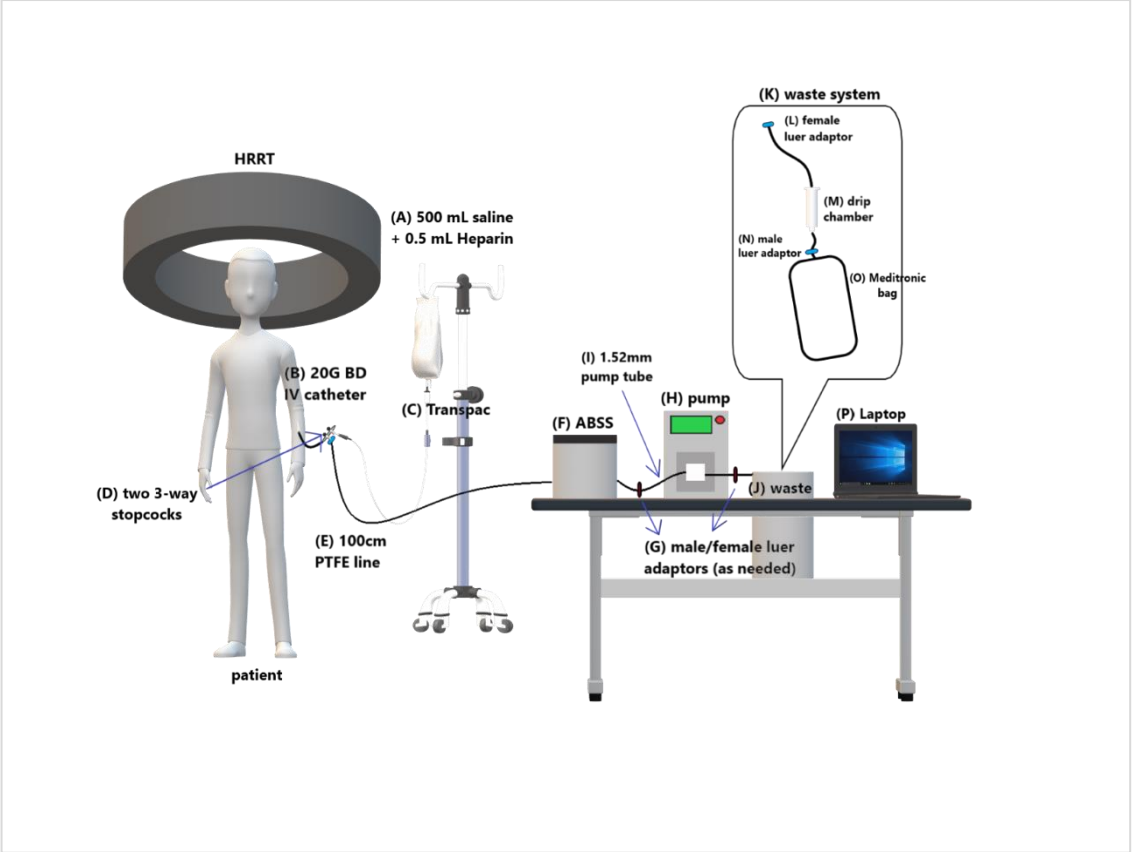

Figure 4. Automatic Blood Sampling System and assembly parts. (A) 500 mL saline + 0.5 mL heparin solution. The bag is pressure cuffed 300 mmHg. (B) IV Catheter, BD Angiocath (20G × 1.88 in). (C) Transpac™ IV monitoring kit with transducer, ICU Medical 42584-05. (D) Two 3-way stopcock connections for saline line, PFTE line, and manual sampling. (E) 100 cm PTFE line, 1.0/2.5 mm with luers, Mediman® 0598. (F) Automated Blood Sampling System (ABSS), PBS-101 Commencer®. (G) Autoclaved Masterflex® 3/32 in male/female barb polypropylene luer adaptors, Qosina® 11535(male) and 11534(female). (H) Ismatec pump, RS-232 20 mA current loop. Rate is set and controlled by specific protocol script on the laptop. Pump is set to withdraw arterial blood from the patient through the ABSS. (I) Autoclaved PharMed® BPT 1.52 mm ID Yellow/Blue/Yellow pump tube, Cole-Parmer RK-95714-36. (J) Leaded waste chamber. (K) Waste system (parts acquired from different kits: L-N; (L) Autoclaved Masterflex® 1/8 female polypropylene luer connector, Qosina® 11536; (M) Drip chamber from Ranger™ Blood/Fluid Warming system kit, Ref. 3M 24200; (N) Autoclaved Masterflex® 1/8 male polypropylene luer connector, Qosina® 11537; (O) Medtronic drainage bag, Ref. 46710. (P) hp Laptop.

3.1.2 Objective B: Hidex AMG

The full characterization of the Hidex AMG (Hidex, Finland) included the investigation into the effect of varying sample volume and defining the optimal range of sensitivity of the instrument. This was achieved by conducting multiple experiments using both ^{18}F and ^{11}C as

gamma-emitting sources. Prior to each experiment, a quality control, and eventually a re-calibration was performed, using a ^{137}Cs activity source (Hidex, Finland, ^{137}Cs Quality Control-3.36 kBq, $t_{1/2}$ = 11,018.3 days, Eγ = 550-750 keV) to get a peak position in the channel corresponding to 662 ±10 keV, a resolution of 10±5% and an efficiency of 18±5% within a 550-750-keV energy window. The stability of the QC measurement was assessed when the crystal of the AMG was allowed to warm up for four hours versus no warm-up time. All ^{18}F samples were counted for 60 seconds unless otherwise stated, using an energy window of 400-600 keV around the 511-keV coincidence peak for ^{18}F.

Each counting acquisition will provide a series of values for individual samples, including counted time, dead time factor, raw counts, counts per minute (CPM). The Hidex AMG interface automatically calculates several outputs. Raw counts are calculated from the spectrum to the 400-600 keV template window using the formula,

$$counts = \sum_{first\ channel}^{end\ channel} counts\ per\ channel$$

Equation 7

The automatic dead time factor (DTF) implemented is determined by the dead time of the instrument and actual activity using the formula,

$$dead\ time\ factor\ (DTF) = \frac{counted\ time}{counted\ time(dead\ time * total\ counts)}$$

Equation 8

The count and dead time factor are used to calculate the counts per minute (CPM) for each measurement using the formula,

$$measured\ CPM = \frac{(background\ corrected)counts}{counted\ time(s)/60} * DTF$$

Equation 9

The AMG will automatically decay-correct CPM to calculate normalized CPM values. This normalized activity is calculated to a time of reference (t_0) usually representing the time and activity of the first sample in the acquisition based on the half-life of radioisotope, using the formula,

$$A_0 = A * e^{-(\frac{\ln(2)\Delta t}{T_{1/2}})}$$

Equation 10

Where, A_0 is the normalized CPM, A is the measured CPM, $T_{1/2}$ is the isotope half-life (109.8 min for ^{18}F, and 20.38 min for ^{11}C) [69], and Δt is the time respect to t_0. The counting efficiency was calculated based on the normalized CPM values and known activity of the sources, using the formula,

$$abolute\ efficiency = \frac{\left(\frac{normalized\ CPM}{60}\right)}{Activity\ (Bq)}$$

Equation 11

For the presentation of the results the activities were expressed in nanocurie (nCi).

3.1.2.1 Experiment 1: Background Correction

The influence of background noise and the effectiveness of the Hidex AMG shielding system was assessed by the repeated measurement of the activity detected from an empty (nonradioactive) sample, positioned next to adjacent radioactive samples in the 13-mm rack. All samples collected were corrected for background noise by subtracting the activity detected from a blank tube from the total activity of each sample. The blank tube was positioned so that it was always the first measurement of each rack counted in the data acquisition and contained no

radioactivity, with all proceeding radioactive samples placed and counted adjacent to the blank measurement. There were no observed significant patterns of change of the background activity counts therefore, the activity across all blank measurements was averaged and used as a single value that was subtracted from the total sample activity to obtain the final background corrected value.

3.1.2.2 Experiment 2: Efficiency of Response

The efficiency of each gamma counting instrument can be highly variable and is dependent on the isotope being measured. An experimental measure of counting efficiency by the Hidex AMG was assessed with the goal of cross-calibrate it with the other devices in the institution for the isotope of interest (^{11}C and ^{18}F).

The cross-calibration between a Capintec™ Dose Calibrator and the AMG was performed to determine the efficiency of the AMG respect to the values read in the Capintec™ Dose Calibrator using a ^{18}F source. The experiment began with the preparation of a 200 mL aqueous solution of 12,000 nCi of ^{18}F. This solution was then used to prepare a total of eight samples of different geometry and volume. Samples included four 3.0 mL aliquots in 4 mL ETDA tubes and four 1.0 mL aliquots in 3 mL polystyrene tubes. Again, the first measurement was reserved for the background count with no activity. Data acquisition was recorded over the course of 35 hrs (n=88 paired measurements), with a counting time of 60 seconds and a decay correction to the time of the initial activity measurement by the synchronized dose calibrator.

To assess the linearity of the response of the Hidex AMG respect of the activity of the sample, the decay per minute (DPM) of the sample given by the dose calibrator was calculated using the half-life of the radioactive decay. The activity measured by the AMG was background

corrected and converted from Becquerels (Bq) to nCi. The percent efficiency was calculated using the formula, [70]

$$\%\, efficiency = \frac{CPM}{DPM} * 100\%$$

Equation 12

The average efficiency for both the EDTA and polystyrene tube were determined to evaluate the optimal range of activity with respect to ^{18}F.

3.1.2.3 Experiment 3: Sample Volume and Geometry

The effect of sample volume on the count rate and relative efficiency of the AMG was assessed using an experiment to analyze samples of ^{18}F with a constant activity and varying volumes. This effect can be attributed to the loss emitted photons that have a greater likelihood of escaping through the hole of the detector well when volume increases (depicted in Figure 3) [12]. The efficiencies for several types of tubes with varying volumes were determined.

a. Validation of Effect.

The experimental design involved the preparation of a 1000 nCi sample of ^{18}F in 1.0 mL aqueous solution. The initial time and activity at production was recorded, and 0.1 mL aliquots of this stock solution was then placed into two 4 mL (13-mm x 75-mm) EDTA blood tubes to make samples an approximate activity of 100 nCi. One additional vial was reserved for the background measurement with no activity. An initial count of 150 sec was acquired for both samples as a reference count rate with low noise. An additional forty 60 sec count measurements were performed, adding a 100 µL aliquot of non-radioactive water to the vials between each measurement. The volume of the sample was gradually increased between each measurement between 0.1 and 4.0 mL, while maintaining the total activity. This data was used to estimate the percent counting efficiency of ^{18}F with respect to varying sample volume.

b. Effect of Volume on Radiometabolite Experiments

These experiments assessed the counting efficiencies of the varying sample volumes and tubes used during plasma radiometabolite analysis. To begin, a radioactive sample of ^{18}F was acquired with a starting activity of 2.24×10^6 nCi in 4.0 mL of aqueous solution. This initial sample was diluted deionized water and mixed thoroughly to create a desired solution with a concentration of approximately 500 nCi/mL. To determine the individual efficiencies of all the possible volumes for the Oasis filter eluents during radiometabolite analysis, eight 4 mL (13-mm × 75-mm) EDTA blood tubes were used with volumes ranging from 0.5 – 4.0 mL, increasing by 0.5 mL between each sample. These samples were measured at five time points to acquire matched duplicate values of efficiency. A similar design was used for the 5 mL polystyrene tubes used to hold the whole blood/plasma aliquots during metabolite analysis. For this step, 0.3 mL radioactive sample was aliquoted into one tube, and a second 0.6 mL sample was aliquoted into a separate tube. Again, these were measured five times to acquire duplicate results to calculate averaged efficiency values between each sample volume.

3.2 Results

3.2.1 Objective A: Efficiency and Calibration Factor of PBS-101 ABSS

Table 1 shows the calibration factor of the ABSS across varying experimental conditions for both coincidence sum peaks at 511 – and 1022 – keV. The values seem to remain constant under different conditions.

Table 1. Experimental measurements of ABSS calibration factor under different acquisition parameters.

Peak ROI (keV)	Experimental Conditions	Count Time (s)	Calibration Factor (CPS/(nCi/mL))
511	Static w/o pump	60	1.20
1022			3.71
511	Static w/o pump, after switching ABSS on/off	60	1.20
1022			3.69
511	Static w/o pump, after moving position of catheter	60	1.20
1022			3.67
511	Static w/o pump	60	1.20
1022			3.61

3.2.2 Objective B: Characterization of the response of the Hidex AMG

3.2.2.1 E1. Background correction

The experiments did not show any systematic pattern of the background counts, including low and constant measurements. Therefore, the background counts across all measurements within a specified acquisition were averaged and subtracted from the counts for the radioactive samples before decay correction. The results confirmed that there is low penetration of the lead-shielding for the environmental radiation.

3.2.2.2 E2. Optimal Range of Activity plot

The results displayed in Figure 3 provide information on the capacity of the NaI crystal detector of the AMG for capturing large volume of positron annihilation events. It is observed in Figure 5 that at high concentrations of activity, the dead time of the detector increases, and

therefore decreasing the precent counting efficiency. On the other hand, at low concentrations of activity, the average counting efficiencies show high levels of variability.

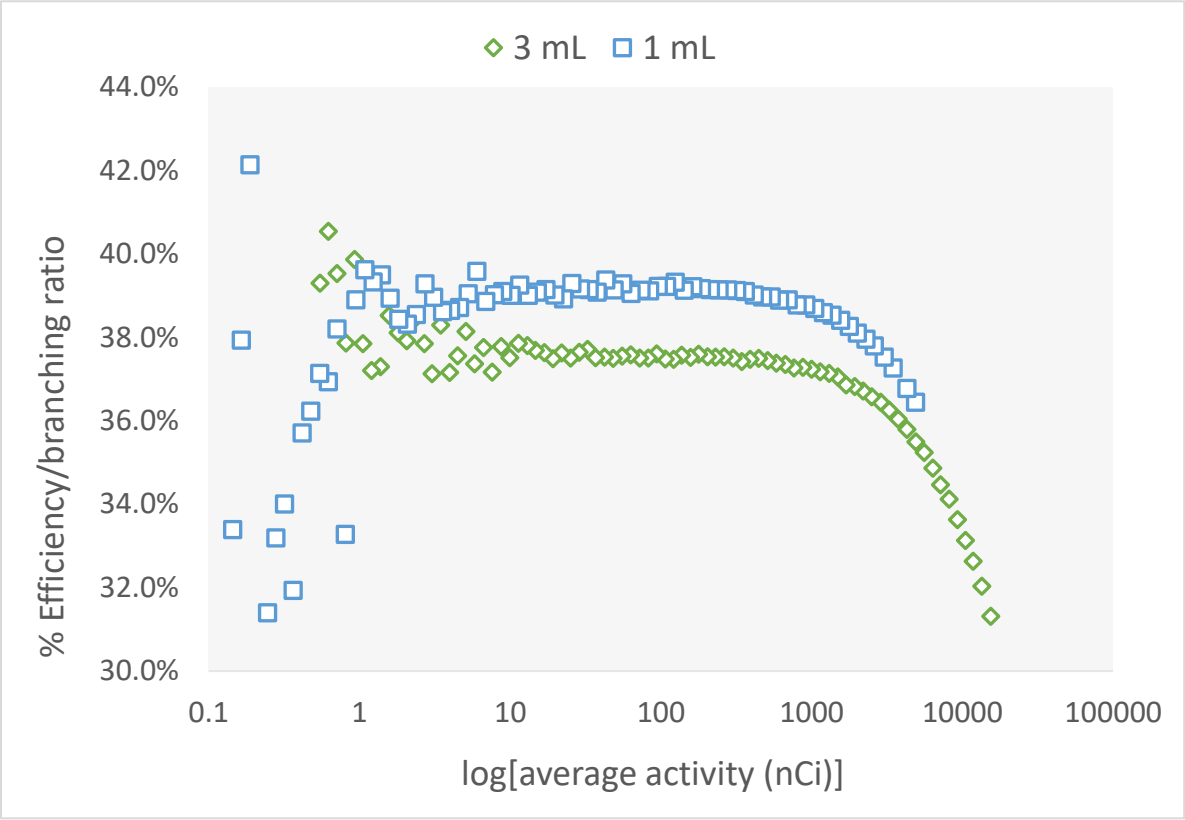

Figure 5. The percent efficiency/branching ratio for ^{18}F, accounting for the radioactive decay of the isotope, as a function of the logarithmic scale of the average activity between the 3 mL and 1 mL samples. Data was acquired in the window centered around the coincidence sum peak (400-600 keV).

From these results, it was determined that the optimal range of activity for the capacity of the AMG detector was observed between 10-500 nCi. The average percent efficiency (mean±SD) corrected for the branching ratio of ^{18}F (0.967) for both the 3 mL and 1 mL samples within the optimal range of sensitivity (10-500 nCi) were determined to be 37.5±0.2% and 39.1±0.4% respectively (Figure 6). Experiment 3 expands on the effect of volume on counting efficiency.

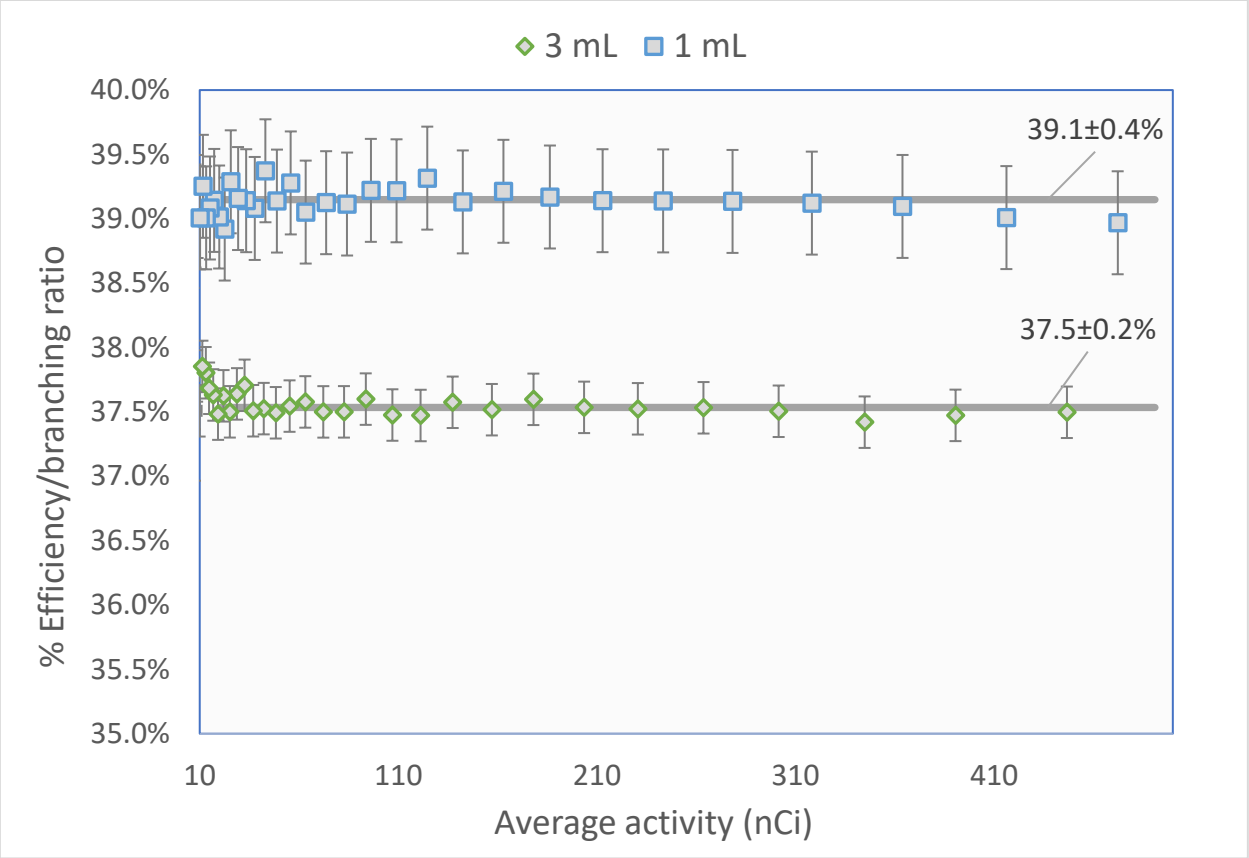

Figure 6. The average percent efficiency/branching ratio for ^{18}F the 3 mL (green) and 1 mL (blue) samples within the optimal range of 10-500 nCi, accounting for the radioactive decay of the isotope. Vials 1-4 consisted of 3 mL aliquots in 4 mL EDTA blood tubes; Vials 5-8 consisted of 1 mL aliquots in 3 mL polystyrene tubes. Data was acquired in the window centered around the coincidence sum peak (400-600 keV).

3.2.2.3 E3. Sample Volume Effect on Relative Efficiency

The average percent efficiency (mean±SD) of the initial 150-s reference measurement between the two samples was determined to be 36.7±0.3% which was used to compare the efficiencies of the following forty measurements. Figure 7 represents the absolute efficiency as a function of increasing sample volume acquired in the window centered around the 511-keV energy window for ^{18}F (400-600 keV). It was observed that there is an increasing likelihood of the escape of photons from the top of the well as sample volume increases, subsequently decreasing the count efficiency for those samples. It is observed in Figure 7 that between 0.1 – 2.0 mL the percent efficiency for both samples of ^{18}F are in close agreeance with the reference measurement with low levels of noise. The average percent efficiency for the two samples were

found to be 35.4±1% and 36.2±1% respectively. Volumes above 2.0 mL begin to have greater dispersion and begin to a decrease in percent efficiency. This observation provides evidence that the optimal range for sample volume is between 0.1 and 2.0 mL for ^{18}F.

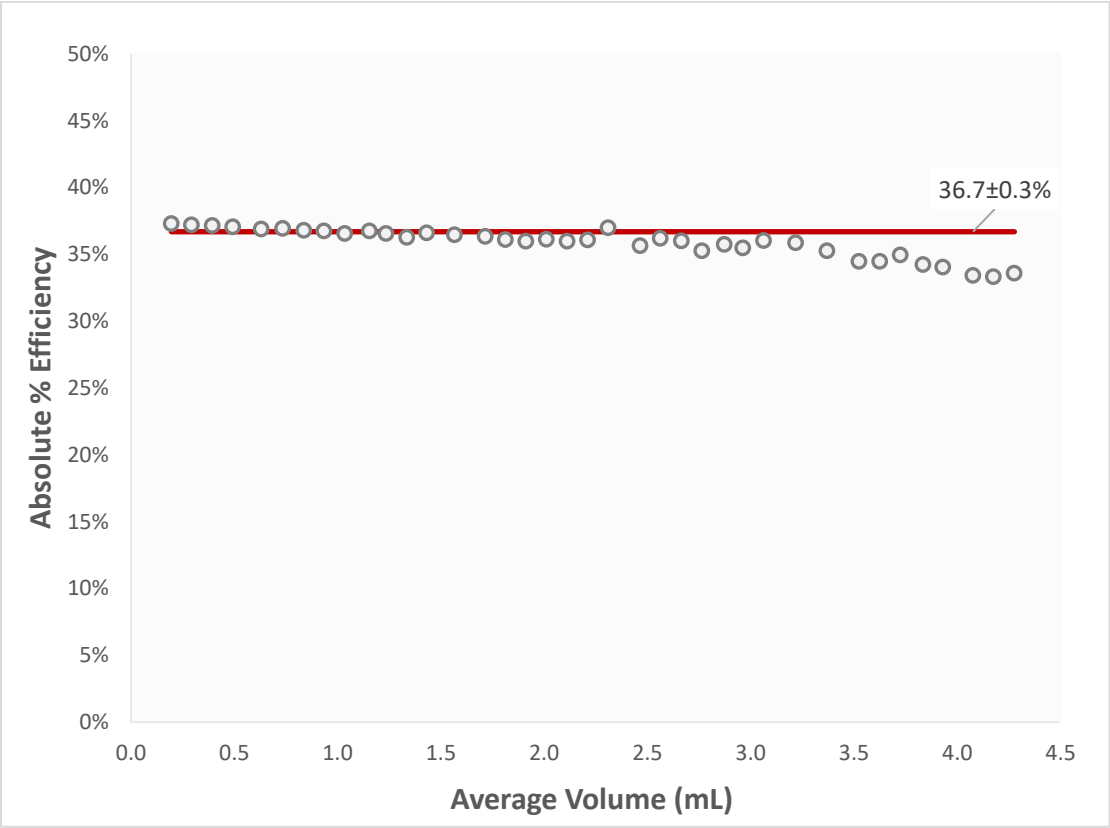

Figure 7. Percent efficiency of the AMG for ^{18}F as a function of sample volume. Two samples of 100 nCi in 4 mL EDTA tubes were measured in the 13 mm × 75 m Hidex racks. Data was acquired in the window centered around ^{18}F 511 keV energy window.

Figure 8 shows the difference in efficiency of the Hidex AMG for ^{11}C in a range of sample volumes from 0.3 – 4.0 mL, representing the various sample sizes required for plasma metabolite analysis during [^{11}C]CURB PET imaging. The average efficiency using a window of energy between 400-600 keV was 32.7%. When using an energy window that is centered exactly ±20% of the 511 keV coincidence peak (409-613 keV), the efficiency stayed relatively stable with an average efficiency of 33.0%.

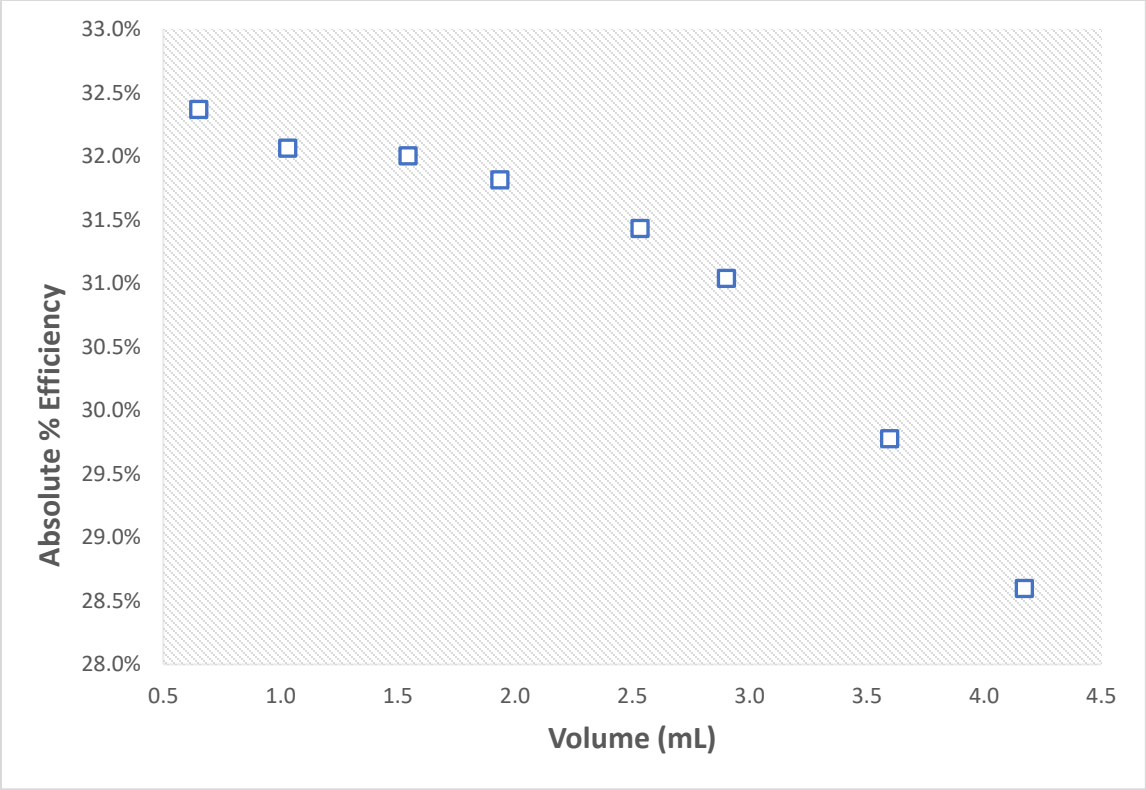

Figure 8. Percent efficiency of the AMG for ^{11}C as a function of increasing sample volume acquired during plasma metabolite analyses.

3.3 Summary

Due to the necessity of additional instruments for obtaining the arterial plasma and radiometabolite activity measurements, there will always be a level of variability and uncertainty introduced to the data across measuring instruments. Through the characterization and rigorous calibration of all gamma counting instruments, including the ABSS and AMG, the uncertainty and error introduced to the data collected can be minimized. The characterization of both the ABSS and AMG instruments used for arterial blood sampling showed that the response of both gamma counters are stable and reproducible with minimal uncertainty.

4. AIM II: The Sensitivity between [^{11}C]CURB Macroparameters

4.1 Methods

4.1.1 Assessment of Sensitivity between Parameters

[^{11}C]CURB macroparameters K_i, k_3, and λk_3 provided by the 2-TCM*i* were compared to predict the difference in patterns of FAAH concentration of people who possess the C/C (n=10) or A/C (n=7) rs324420 FAAH gene.

To assess the sensitivity between macroparameters to detect differences in FAAH concentration in a large ROI versus a small ROI, the values for K_i, k_3, and λk_3 were compared between C/C and A/C subjects using independent sample t-test (two-tailed, α=0.05). This was computed using two ROIs: (1) the temporal cortex (large ROI) and (2) the dorsal caudate (small ROI). Independent t-tests (α=0.05, two-tailed) between C/C and A/C groups were performed using RStudio (RStudio Team (2020). RStudio: Integrated Development for R. RStudio, PBC, Boston, MA, United States). The percent difference of the indices for FAAH levels, K_i, k_3, and λk_3 between the genetic groups and the Cohen's *d* (α=0.05) values were determined for both ROIs.

Mean values and standard deviation of the indices calculated in the previous experiment were used with Monte Carlo simulations (α=0.05, simulations = 2000, sample size per group from n=2 to n=100) to perform a sample size calculation (number of subjects per group) required to detect a 15%, 20% 25% theoretical reduction in FAAH in potential clinical experiments. The Monte Carlo simulation were written in MATLAB (MATLAB 2022b, The MathWorks, Inc., Natick, MA, United States). Two thousand MC simulations were performed for each sample size n per group per genotype and the percent of simulations with $p<0.05$ in an ANOVA test were

recorded. The sample size requires was that producing in 95% of the simulation a $p<0.05$. The code used can be found in *Appendix I.b*.

4.1.2 Dataset

The present study was performed with data of 17 healthy volunteers (HVs) included in previous publications [27, 32, 33, 37]. Only HVs, who tested negative for THC on a urine drug screen, were considered as cannabis use has shown to affect [^{11}C]CURB binding [32, 44].

4.2 Results

The significance (*P* values) of the parameters estimated by the 2-TCM*i* in the temporal cortex between C/C and A/C genotypes indicated that all three, K_i, k_3, and λk_3, were successful at detecting the changes in FAAH levels. k_3 showed the strongest statistical difference (P=4.18e10^{-5}, Cohen's *d* 2.81), followed by λk_3 (P=0.002, Cohen's *d* 1.91), and to a lesser extent K_i, (P=0.021, Cohen's *d* 1.27) (Figures 9-11). The percent difference between C/C and A/C genotypes were 13.7%, 19.9%, and 25.6% estimated by K_i, k_3, and λk_3 respectively.

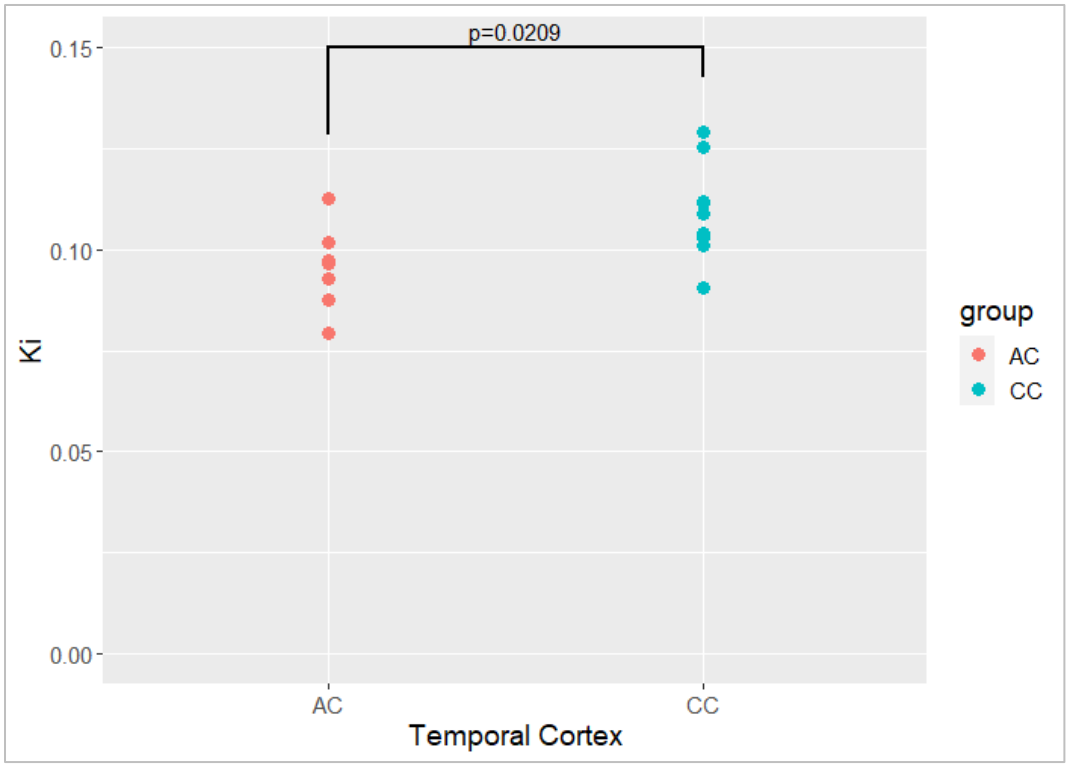

Figure 9. Independent t-test (α=0.05, two-tailed) using K_i values from the temporal cortex between C/C and A/C genotypes (*P* = 0.209).

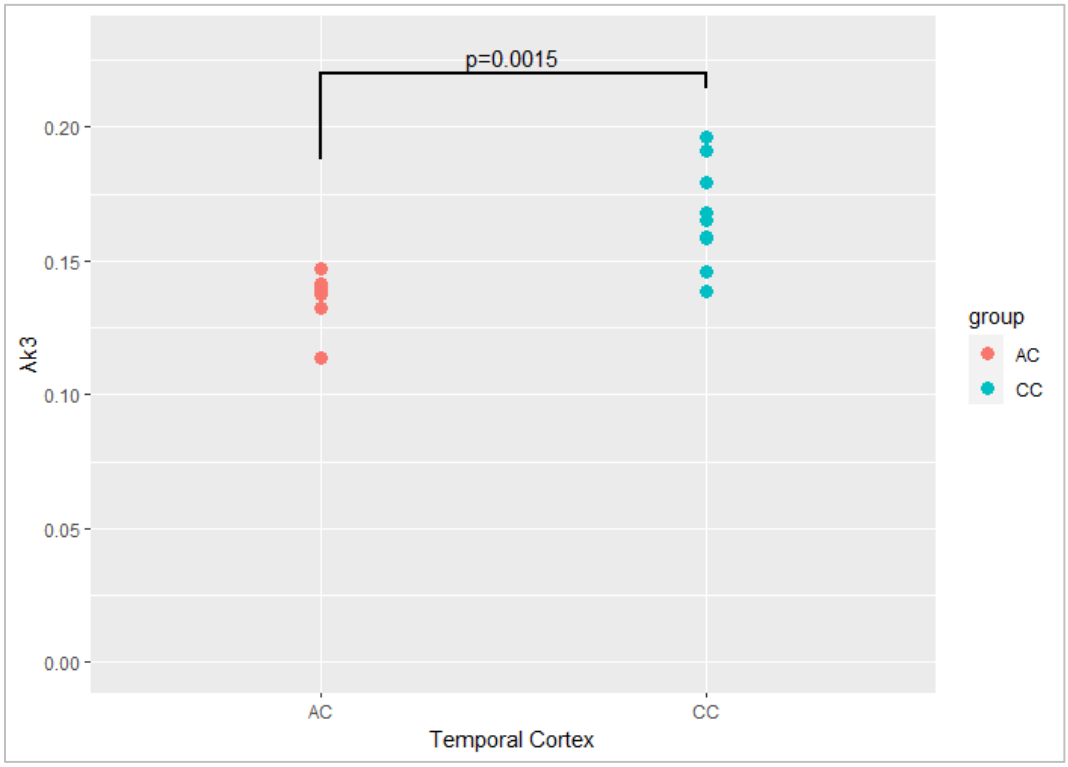

Figure 10. Independent t-test (α=0.05, two-tailed) using λk_3 values from the temporal cortex between C/C and A/C genotypes (*P* = 0.0015).

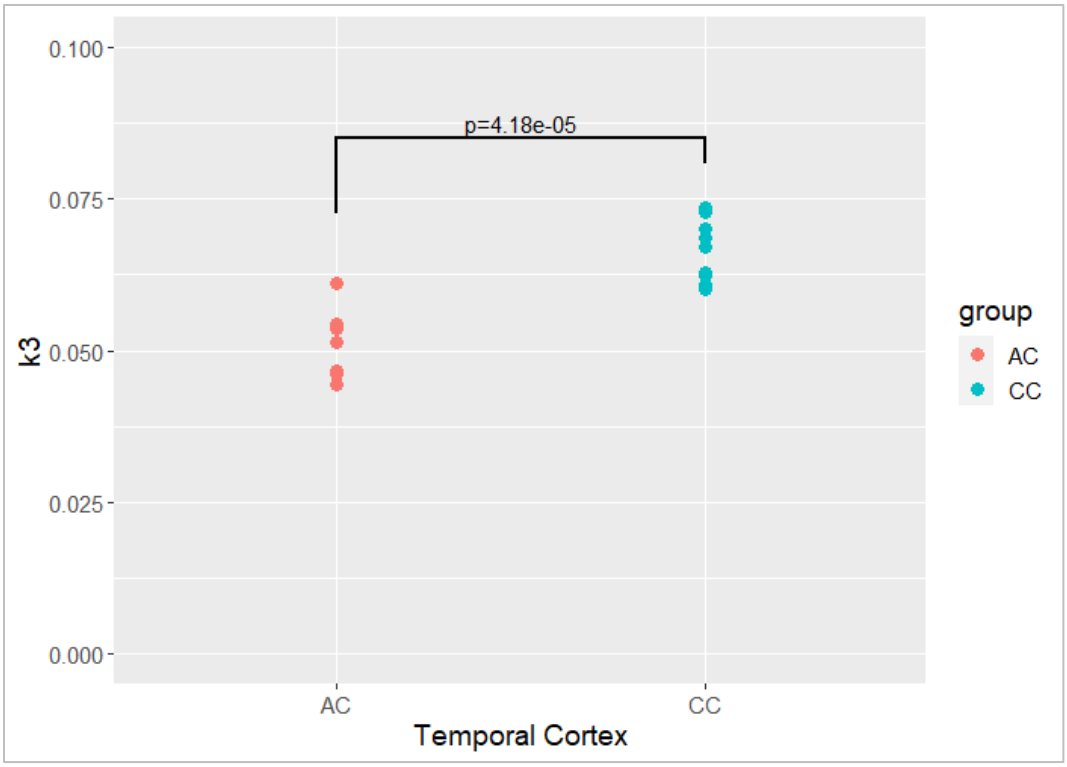

Figure 11. Independent t-test (α=0.05, two-tailed) using k_3 values from the temporal cortex between C/C and A/C genotypes (P = 4.18x10^{-5}).

The results when performing the same analyses but using the dorsal caudate indicated that all three were again successful at detecting the changes in [FAAH] with λk_3 (P=0.0002, Cohen's d 2.36) demonstrating the highest statistical difference, closely followed by k_3 (P=0.0009, Cohen's d 2.02), and to a lesser extent K_i, (P=0.012, Cohen's d 1.40) (Figures 12-14). The percent difference between C/C and A/C genotypes when using K_i, k_3, and λk_3 as an index were 16.3%, 29.9%, and 25.9% respectively.

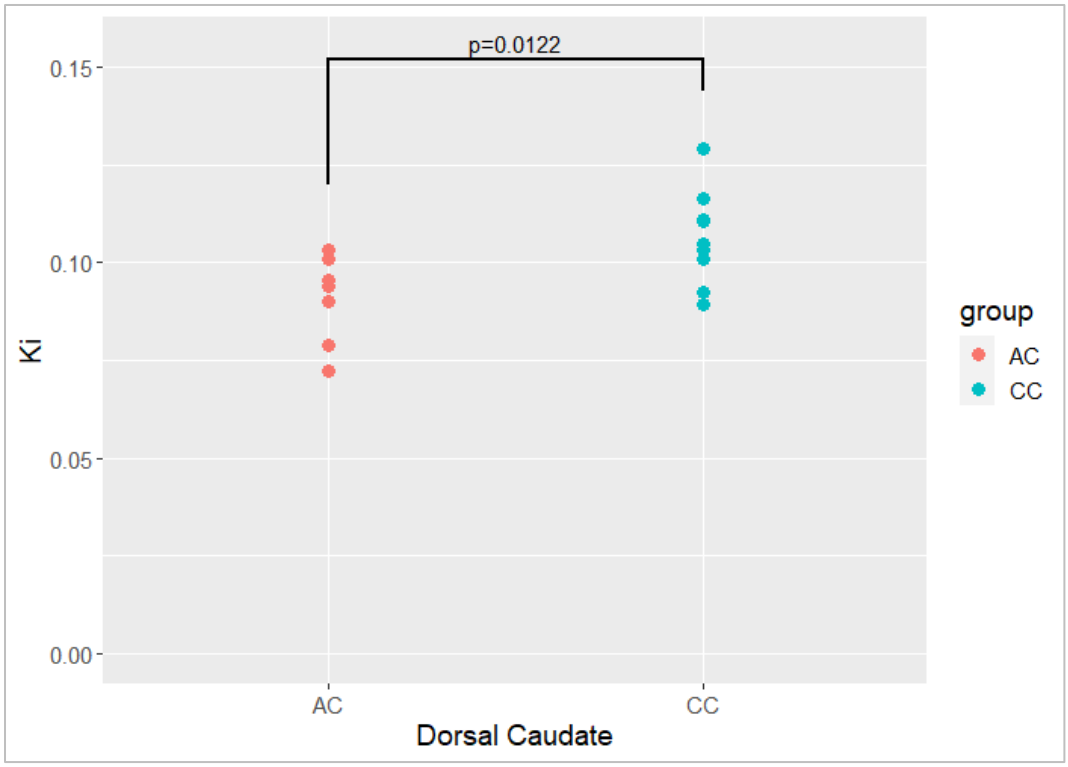

Figure 12. Independent t-test (α=0.05, two-tailed) using K_i values from the temporal cortex between C/C and A/C genotypes (*P* = 0.0122).

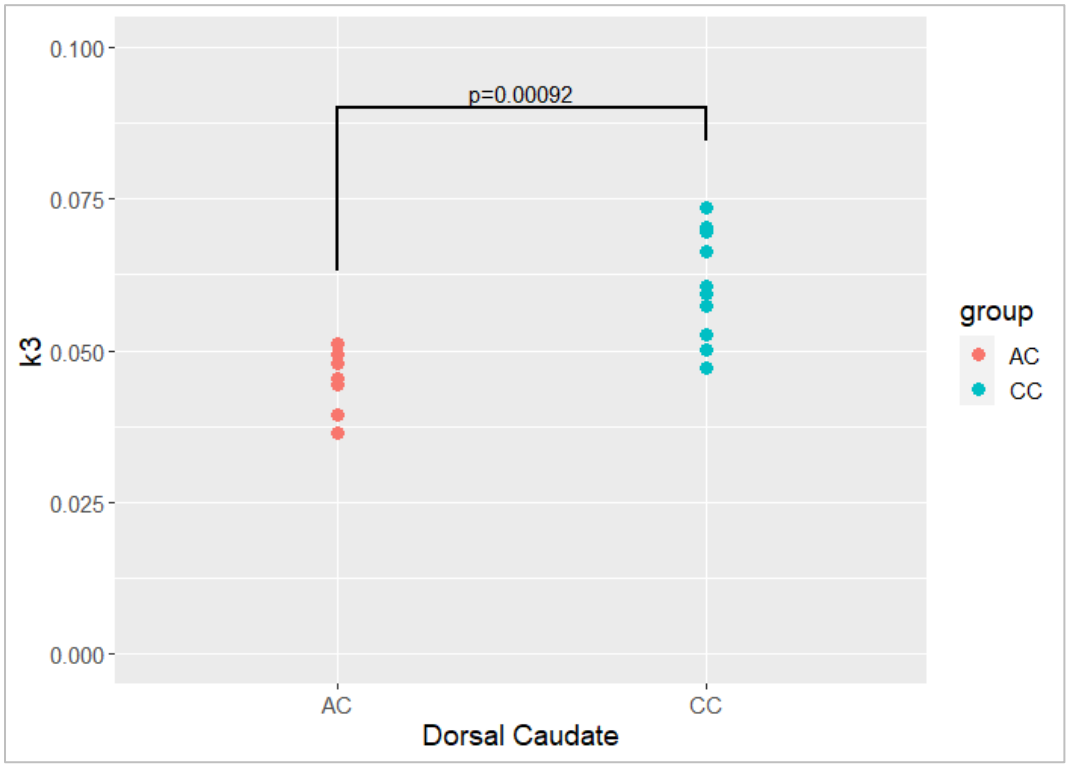

Figure 13. Independent t-test (α=0.05, two-tailed) using k_3 values from the dorsal caudate between C/C and A/C genotypes (P = 0.00092).

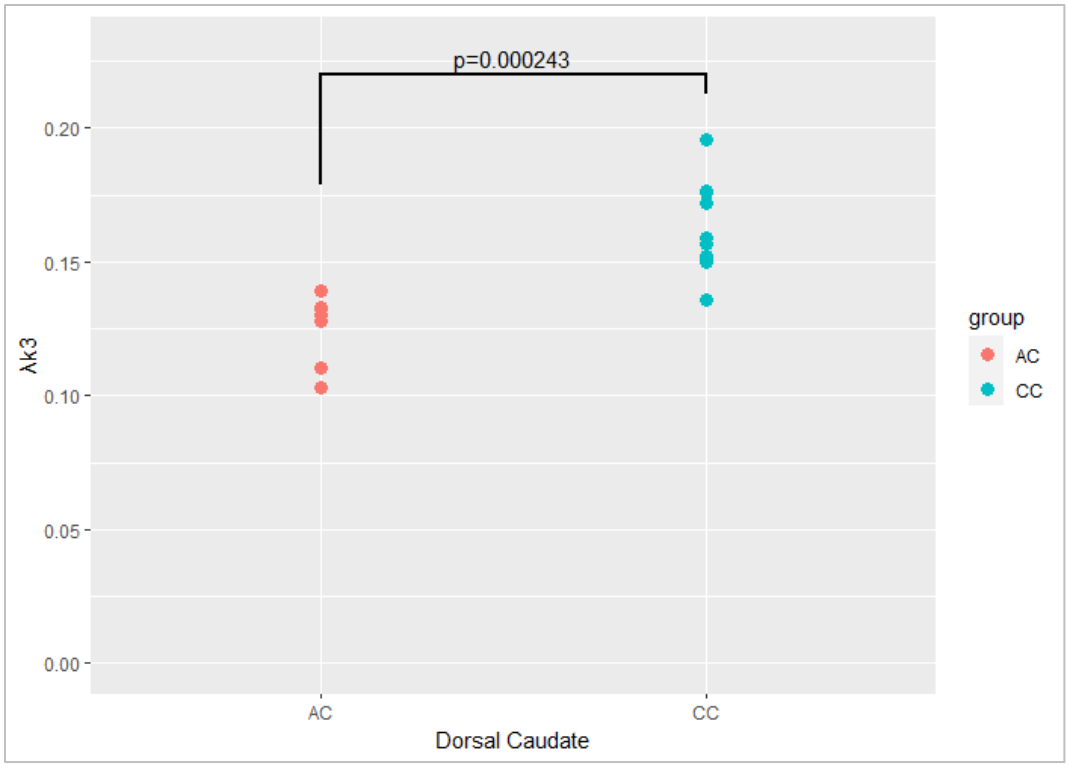

Figure 14. Independent t-test (α=0.05, two-tailed) using λk_3 values from the temporal cortex between C/C and A/C genotypes (*P* = 0.000243).

The mean values and standard deviation were used to predict the samples size required to detect a theoretical 15%, 20% 25% reduction in FAAH levels in a potential clinical experiment (Figure 15) for each parameter. Figure 15 indicates that λk_3 and k_3 have better sensitivity and smaller sample size requirements for detecting changes in [FAAH], while K_i has lower sensitivity and requires much higher group sizes to obtain the same significance. The results support the first hypothesis that k_3 would have the highest sensitivity for detecting change in [FAAH] in a large ROI such as the temporal cortex.

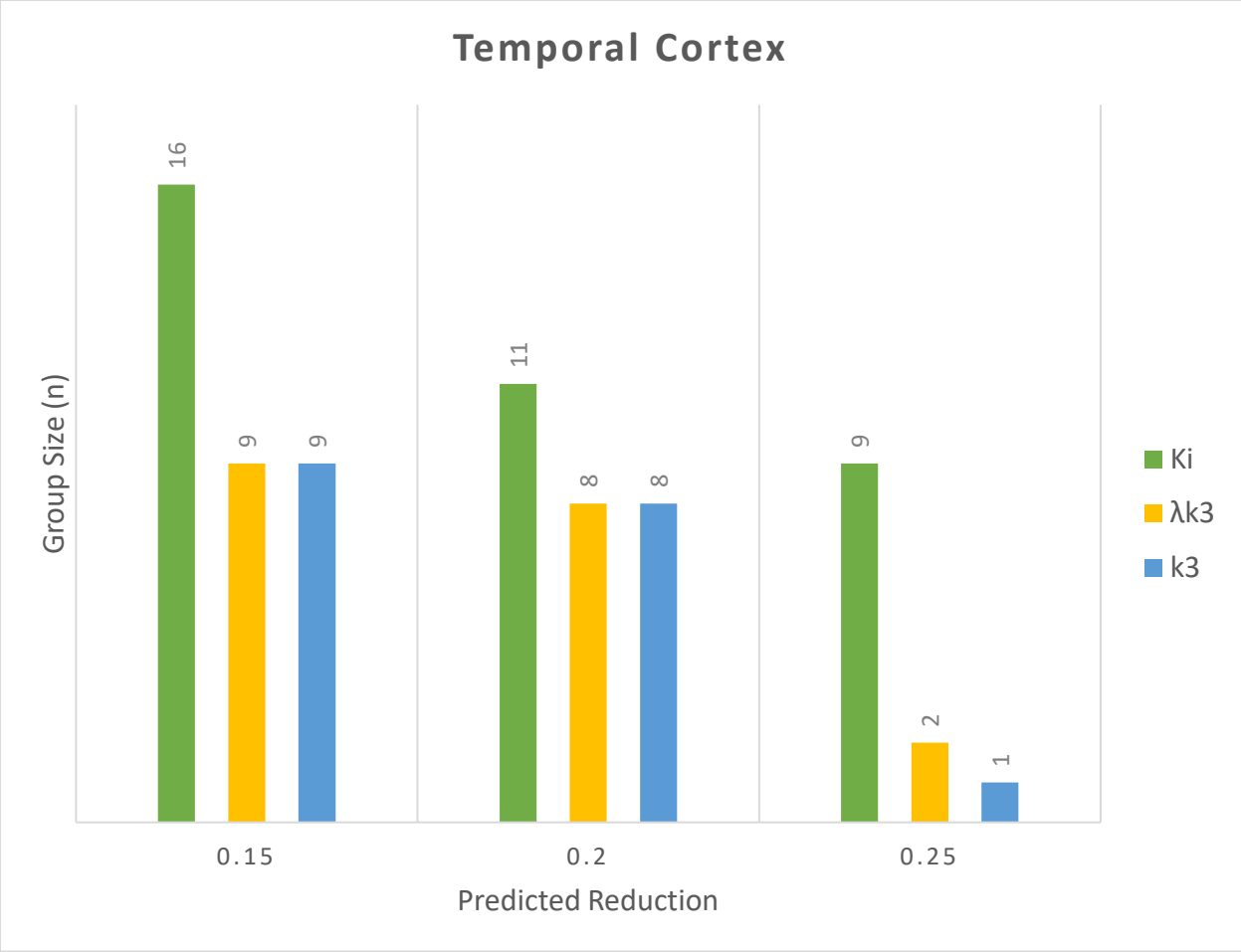

Figure 15. Estimated group sizes between K_i, k_3, and λk_3 in the temporal cortex using Monte Carlo simulations (α=0.05, simulations = 2000, max n = 100) to detect a theoretical 15%, 20% 25% reduction in FAAH.

The predicted group sizes between each parameter shown in Figure 16 provides support that λk_3 has the best sensitivity for detecting changes in [FAAH] in a small ROI such as the dorsal caudate. k_3 surprisingly had almost the exact level of sensitivity despite the precited influence of higher levels of noise in the dorsal caudate. This observation is supported by the higher effect size determined for k_3 (Cohen's *d* 2.02), which is comparable to the effect size of λk_3 (Cohen's *d* 2.36). K_i has shown to have good identifiability [2], but has much worse sensitivity for detecting changes and requires significantly larger sample sizes to have the same significance compared to k_3 and λk_3. The results support the first hypothesis that λk_3 would have

the highest sensitivity for detecting change in a small ROI that is more subjected to higher levels of uncertainty.

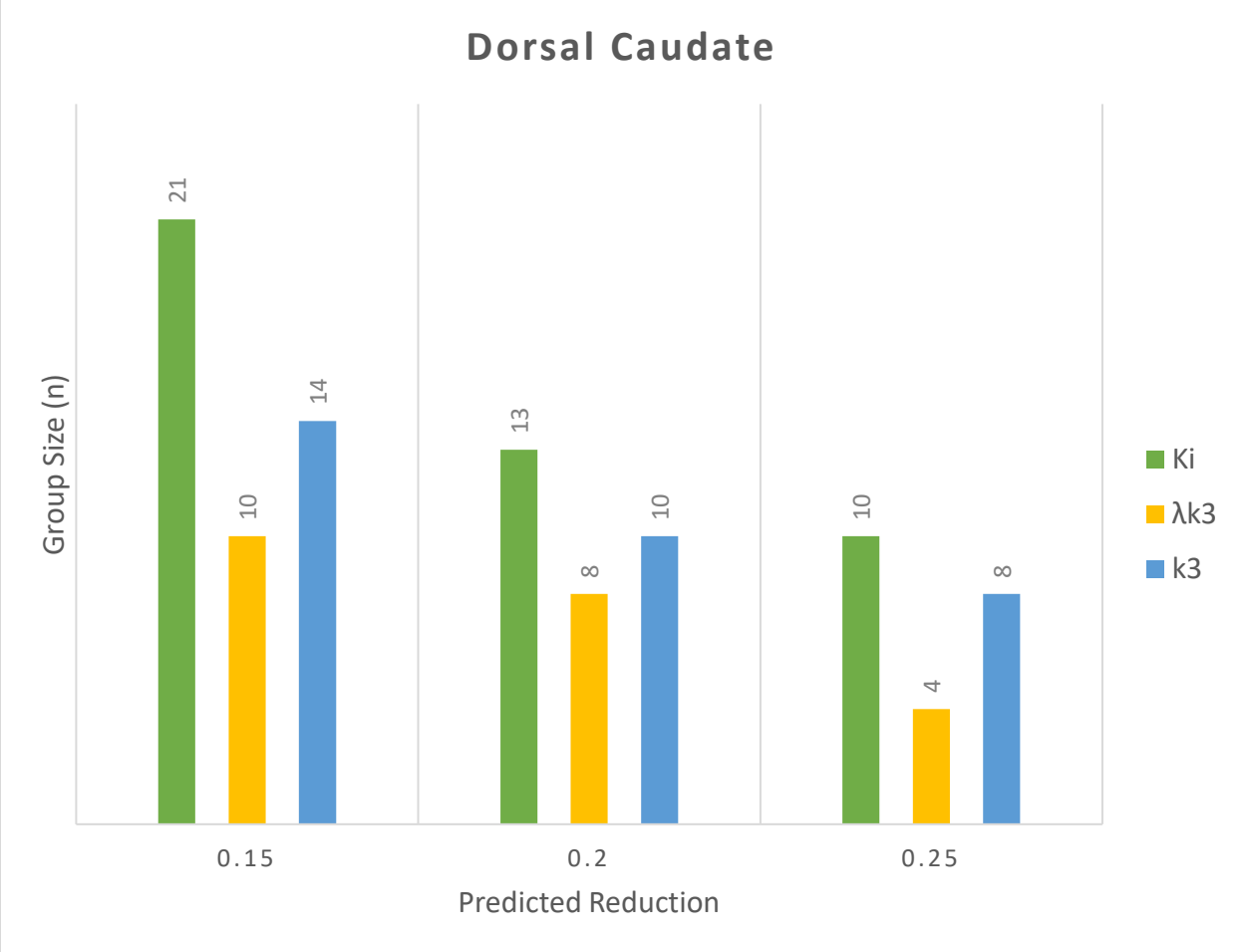

Figure 16. Estimated group sizes between K_i, k_3, and λk_3 in the dorsal caudate using Monte Carlo simulations (α=0.05, simulations = 2000, max n = 100) to detect a theoretical 15%, 20% 25% reduction in FAAH.

4.3 Summary

The results supported both hypotheses that (1) k_3 is a better parameter for indexing [FAAH] in larger ROIs and (2) λk_3 would have the highest sensitivity. In addition, the identifiability between the three parameters in both the temporal cortex and the dorsal caudate further supports the initial hypotheses. Based on a previous study into the FAAH genotype effect, there is a statistically significant reduction in [FAAH] in subjects with the A-allele [66]. The percent

difference between the A/C and C/C was underestimated in both ROIs using K_i due to its non-linear dependence on k_3. The percent difference when using k_3 and λk_3 was more sensitive in detecting this change that is consistent with the previous studies, although in the temporal cortex both parameters detected larger percent differences than previously reported. In summary, these results indicate that K_i is not a convenient parameter to detect differences in FAAH levels, as the effect sizes expected are smaller than those from λk_3 and k_3. The parameters k_3 and λk_3 are more sensitive to changes in FAAH levels in the brain. The level of noise within a specified ROI will (1) determine the between subject variability and (2) what parameter will present a greater effect size. This result is consistent with the experiments of test-rest based on 6 subjects with >1 month between scans: for cortical ROIs k_3 present better percentage test-retest variability (TRV%) than λk_3. On the other hand, for subcortical ROIs this trend is revered, where λk_3 presents better TRV% compared to k_3.

5. AIM III: Average Peak Input Function (APIF)

5.1 Methods

5.1.1 [^{11}C]CURB Quantification

The TACs for each brain ROI were extracted using an in-house imaging pipeline, that was previously validated as a method for [^{11}C]CURB *in vivo* binding [2, 68]. To begin, the nonlinear transformation to match the standard brain template (ICBM/MNI 152 PD) to the individual high-resolution MR image of the subject that we want to analyze is calculated using statistical parametric mapping (SPM8). The calculated nonlinear transformation is applied later to a set of regions of interest previously delineated in the standard brain template. The subject MR image is then segmented to differentiate gray matter, white matter, and CSF. The set of transformed ROIs is refined based on gray matter probability of voxels of the individual subjects MRI images. The MRI images are then co-registered to the subjects averaged PET image with a rigid body transformation. This new transformation is applied to re-slice the individualized ROI to mask the PET images. The masked dynamical PET images are used to create the TACs for each ROI. λk_3, an index of [^{11}C]CURB binding in a ROI, that has been validated as proportional to the concentration of FAAH in the brain [2, 72], is computed from the TAC and the IF using the 2TCM*i*.

5.1.2 Dataset

This experiment was performed with images previously acquired that were presented in ref [42, 43], including both healthy volunteer's (HVs, n=9) and those who are at clinical high risk for psychosis (CHR, n=10) carrying either the C/A or C/C FAAH polymorphism. As the shape of the peak of the input function would depends on the shape of the bolus, it is important to note that the radioligand was injected with an injection pump (Harvard Apparatus, Holliston,

MA, USA) as a 1-minute bolus. Arterial input functions were created by merging the information of ABSS and manual samples using a Hill function, as described in Pablo Rusjan *et al*. (2013) IFs were delay and dispersion corrected with respect to the radioactivity in blood that would be measured in the FOV [2].

5.1.3 Algorithm for the creation of the APIF and Re-Estimation of λk_3

To begin, the area under the curve (AUC) of the individual input functions were determined at various time points of arterial measured input function (AIF) of each subject to verify there were no significant differences between groups (HV A/C, HV C/C, CHR C/A and CHR C/C). Once this is verified, an average of the AIF expressed in SUV (normalization based on injected dose/weight) across all subjects were computed and the peak between 0 and 15 minutes after injection was kept, creating the plasma-average peak (PAP). Secondly, a biexponential function ($a * e^{bt} + c * e^{dt}$) was used to fit the activity concentration measurements in the manual samples of [^{11}C]CURB in plasma for each subject. Due to the rapid changes and variation in metabolization per individual during the first 12 minutes after bolus injection, the biexponential interpolation is more successful in accurately modeling the manual samples after the 12-minute mark. Therefore, the interpolation was weighed such that the only the samples after 12 minutes were relevant: the time points 3-7 minutes were weighted with a factor of 0.001 and the remaining time points 12-60 minutes were weighted with a factor of 100. For each subject APIF was calculated by merging a rescaled PAP up to 15 min with the biexponential fitted between 15 min and 60 min. The sample at 15 min was used to rescale the PAP such that it was equal to the biexponential fitted value at that time point. The variable time of injection between participants was accounted for. The same procedure was used to create an average peak whole-blood function (APWB). The algorithm was automatized using a script in

Python (*Appendix I.a*). The λk_3 values for each subject were re-estimated using the 2-TCM*i* with the generated APIF and APWB using an in-house kinetic modeling software, fmod.

5.1.4 Sensitivity of AIF vs. APIF for detecting *FAAH* rs324420 polymorphism Effect

To assess the FAAH polymorphism effect between groups, the difference between means of λk_3 values estimated using the measured AIF versus the APIF were calculated using the student's two-tailed t-test for groups of unequal size and equal variance. Variance between groups was determined using one-tailed F-test between the two-sample means. Bland-Altman tests were performed using the temporal cortex, dorsal caudate nucleus, and dorsal putamen as the ROIs to assess biases and variability introduced to macroparameters computation between the AIF and APIF method [75].

5.1.5 Estimated Group Sizes between AIF and APIF

Monte Carlo simulations (*Appendix I.b*) (α=0.05, simulations = 2000, max n = 100) were computed to estimate group sizes (accounting for C/C and A/C subjects) required to detect a theoretical 10%, 15%, 20% 25% reduction in FAAH levels in a potential clinical experiment. Two thousand simulations using MATLAB 2022b (The MathWorks, Inc., Natick, MA, United States) were performed for each sample size between 2 and 100 subjects per genotype per clinical group. The mean and SD resulting from the Section 5.1.4 were used as the HV values for the MC simulations. The group mean minus the theoretical reduction was used to represent the study group in the MC simulations, and the same SD was used between the control and study groups.

5.2 Results

Bland-Altman analyses (Figures 17-19) using λk_3 values from the temporal cortex, dorsal caudate nucleus, and dorsal putamen indicated that there were no significant biases between the AIF and APIF methods. The limits of agreement (LOA) were calculated between measurements to define the limits using +2 standard deviation (SD) to demonstrate a 95% confidence interval (CI; precisely defined: mean ± 1.96 standard deviations), this generates the upper LOA (mean + 1.96 x SD) and lower LOA (mean - 1.96 x SD). LOAs are shown as dotted, red lines with 95%, and bias as solid, gray line.

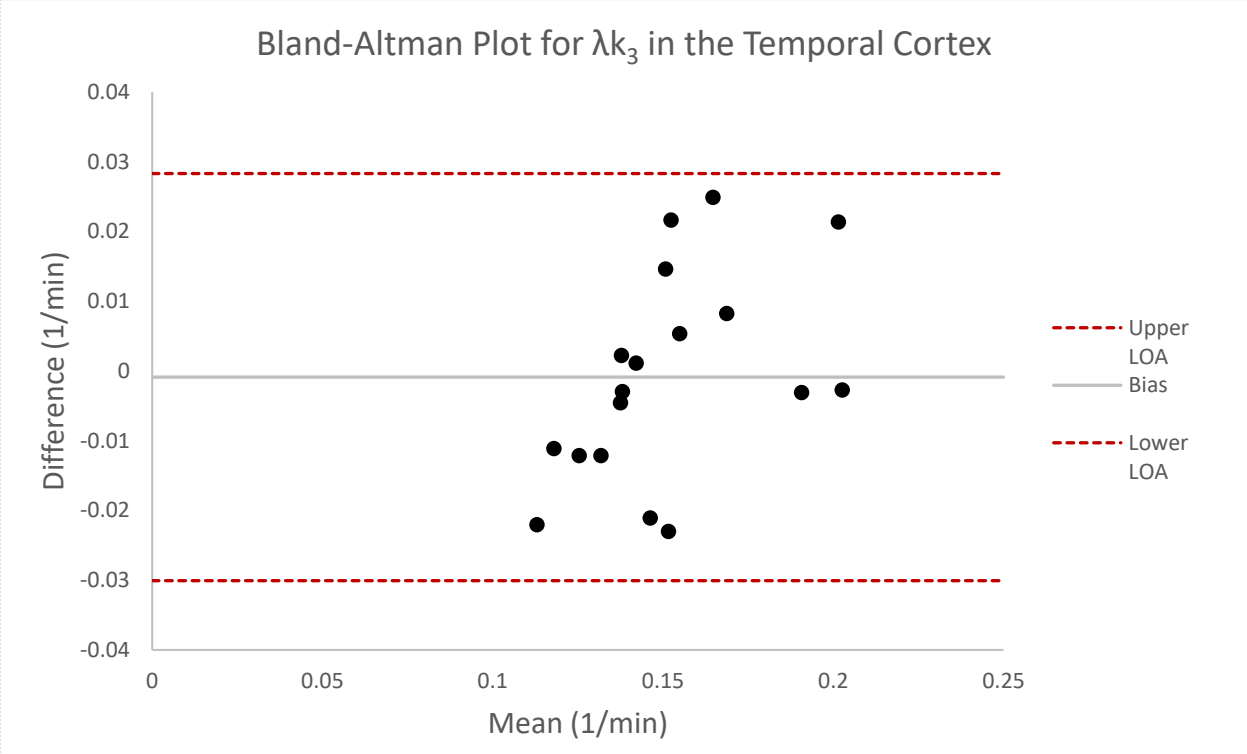

Figure 17. Bland-Altman plot of λk_3 values in the temporal cortex between APIF and AIF. Bias (difference) = 0.0009, Upper LOA = 0.0283, Lower LOA = -0.0301.

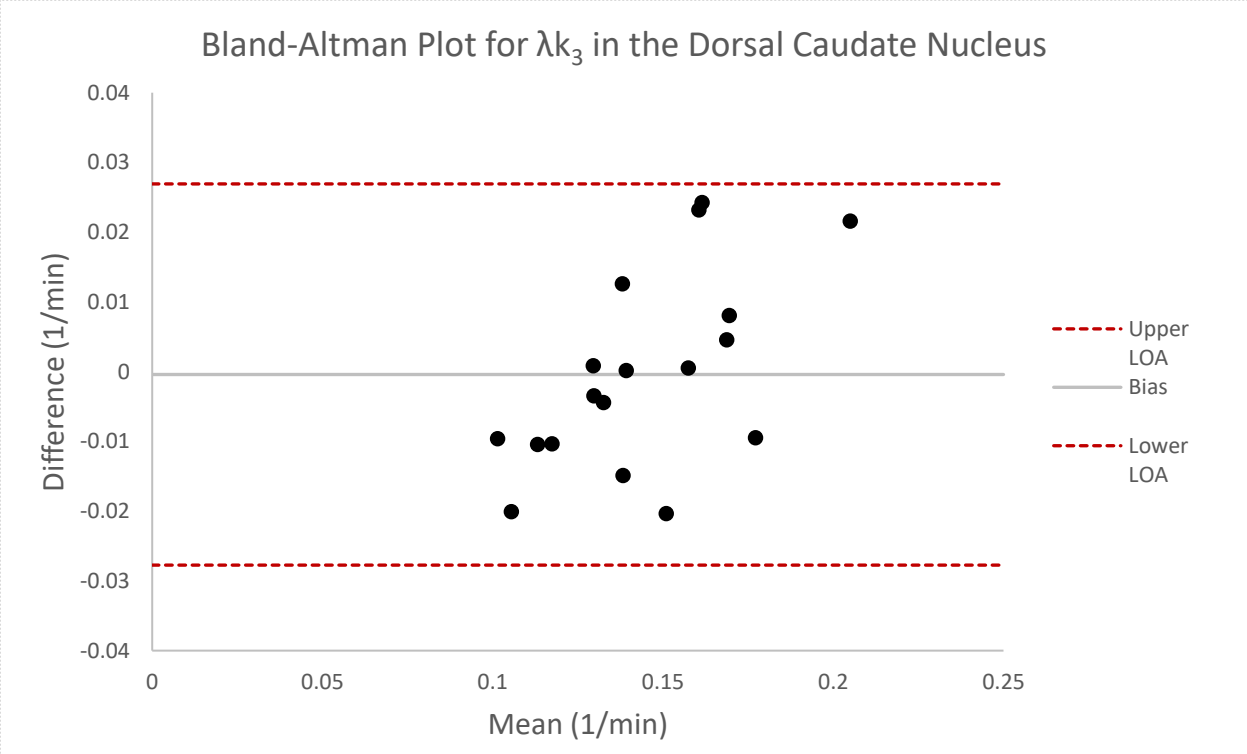

Figure 18. Bland-Altman plot of λk_3 values in the dorsal caudate between APIF and AIF. Bias (difference) = 0.0004, Upper LOA = 0.0269, Lower LOA = -0.0277.

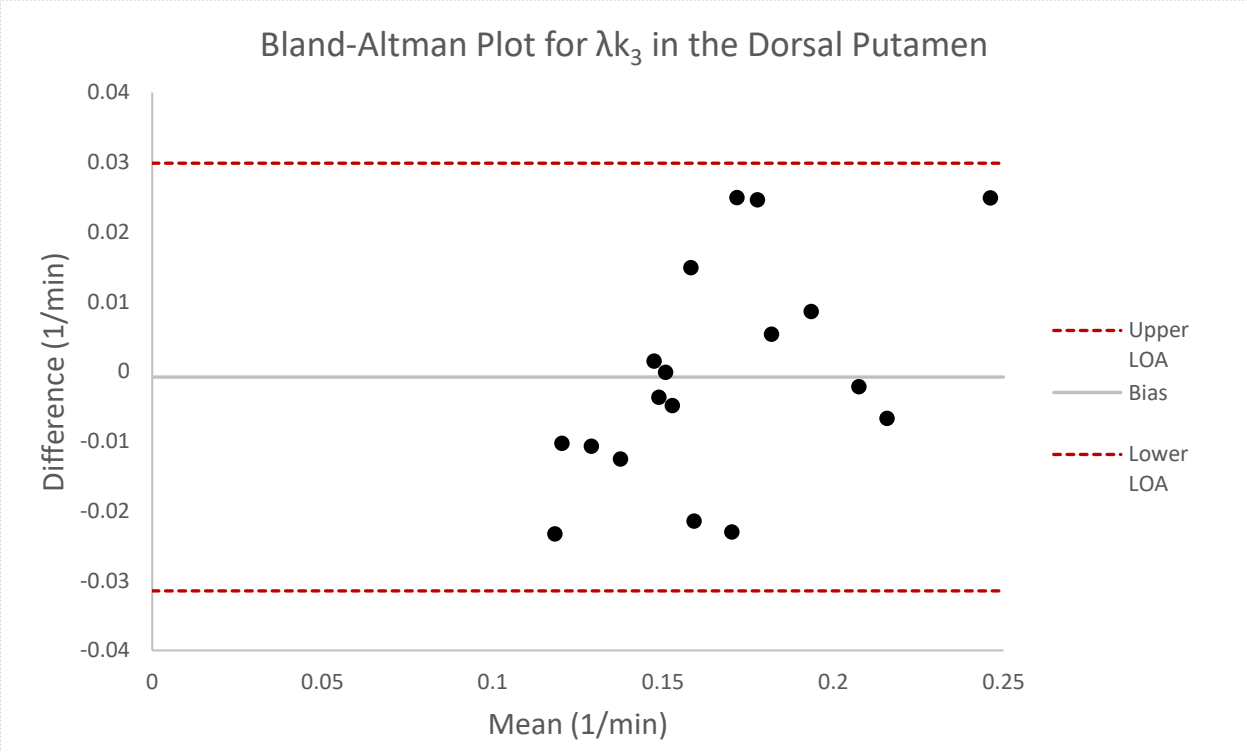

Figure 19. Bland-Altman plot of λk_3 values in the dorsal putamen between APIF and AIF. Bias (difference) = 0.0008, Upper LOA = 0.0299, Lower LOA = -0.0315.

AIF and APIF showed a significant difference in λk_3 values (P=0.0003 and P=0.0234 respectively) due to the polymorphism effect between C/C and A/C (Figure 20). However, the effect size was smaller for the APIF (Cohen's d 0.96) compared to the AIF (Cohen's d 1.70) caused by higher levels of inter-subject variability of the APIF.

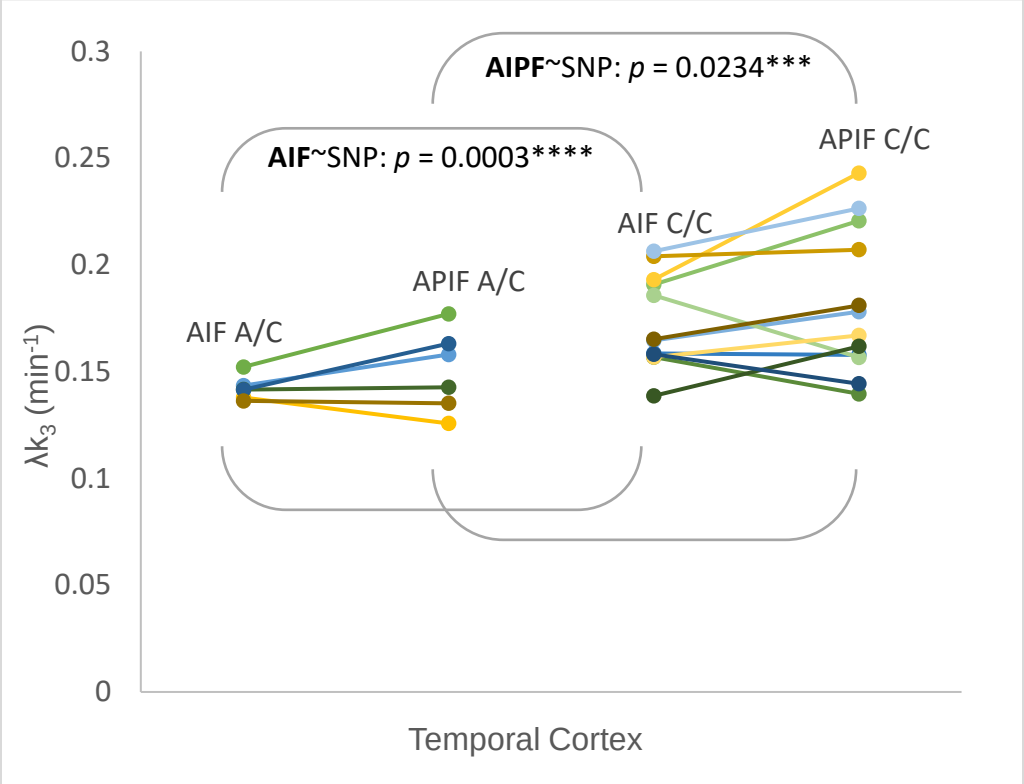

Figure 20. Comparison of the sensitivity between the AIF and APIF methods for detecting the effect on [FAAH] with the addition of an A-allele. The difference detected by the AIF (P=0.0003) is more significant than the difference detected by the APIF (P=0.0234).

To build upon the sensitivity of using the APIF-method opposed to the AIF-method, estimated group sizes to detect theoretical reductions in [FAAH] between the two were determined. The results show that the sample size required to find a significant difference between groups are around double the size for APIF than for AIF (Figure 21).

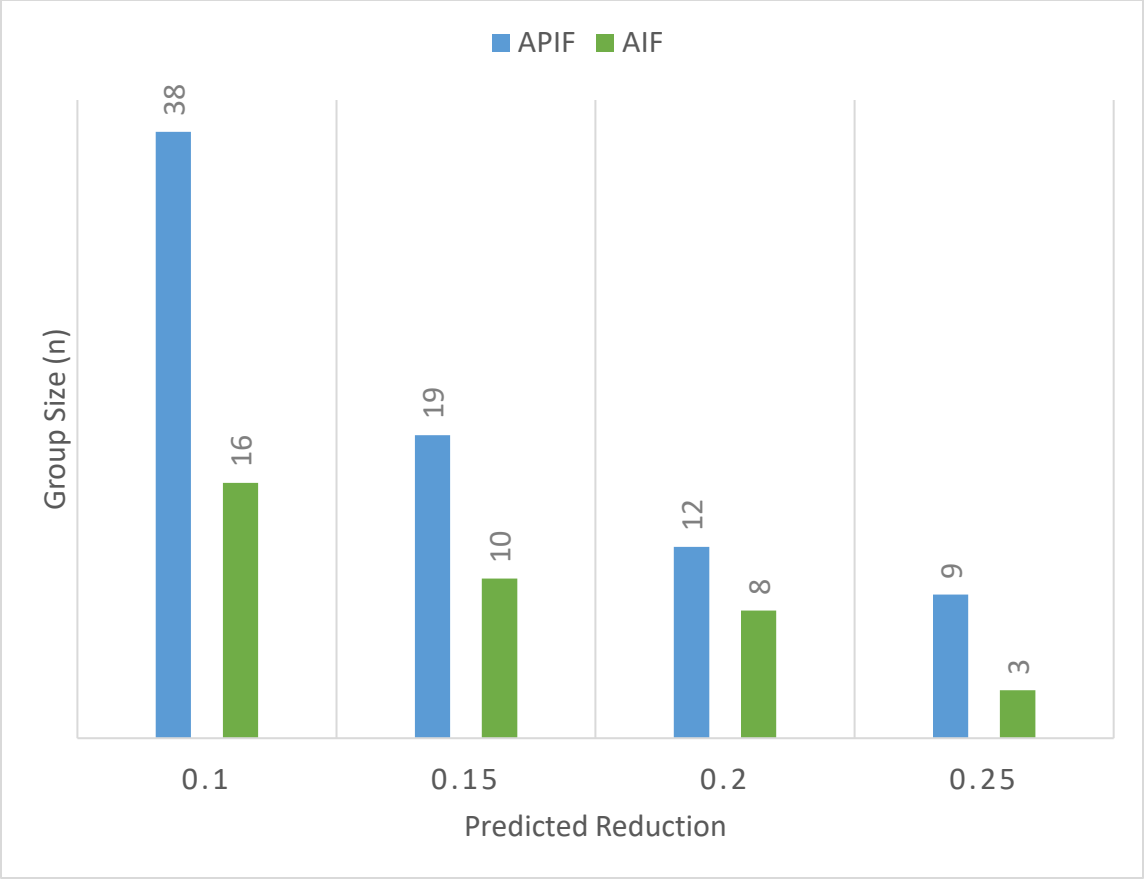

Figure 21. Estimated group sizes for the AIF and APIF methods using Monte Carlo simulations (α=0.05, simulations = 2000, max n = 100) to detect a theoretical 10%, 15%, 20% 25% reduction in FAAH. The AIF method requires smaller samples sizes to obtain significance compared to using the APIF method.

5.3 Summary

The sensitivity of the APIF method for the estimation of 2-TCMi parameters was lower than the method of acquiring individual automated IFs. While using the APIF modeling approach did not produce any significant biases, using an averaged peak fails to capture the rapid changes in the IF during the first 15 minutes post bolus injection and produce a higher inter-subject variability in λk_3. Therefore, it will require larger sample sizes to try to find the same difference between clinical conditions. This highlights the importance of the individual information about the availability of parent compound during the first 15 minutes post injection. In summary, the results demonstrate the importance of acquiring individual ABSS measurements for creating the AIF.

6. Discussion

The present study sought to optimize the technical performance, characterization, and evaluate the stability of required instrumentation for radioligand quantification using arterial blood sampling methodologies.

6.1 Characterization of Instruments used for Arterial Sampling

Aim I of this study investigated the performance of the gamma counting instruments used for the measurement of activity in arterial blood sampling for [^{11}C]CURB. The first sub-objective of Aim I assessed the response of the PBS-101 ABSS under different sampling conditions. The varying experimental conditions were designed to test the optimal length of time required for the BGO crystal detector of the ABSS to warm-up and whether the suggested 2-hr window [11] was sufficient. In addition, the experiments were designed to be able to assess the influence of the counting efficiency during any unexpected events, including the ABSS switching off and back on, or moving the position of the catheter. Also, it was to study whether static radioligand in the catheter could produce a difference in the calibration factor compared to radioligand flowing in the catheter. A difference between the calibration factors could suggest an accumulative adhesion of the radioligand to the walls of polytetrafluoroethylene (PTFE) tube (Figure 4, Part E, Section 3.1.1) [76]. The average cross-calibration factor across all four experimental conditions for the 511 – and 1022 – keV peak ROIs were determined to be 1.20±0.001 CPS/$\frac{\text{nCi}}{\text{mL}}$ and 3.67±0.039 CPS/$\frac{\text{nCi}}{\text{mL}}$ respectively. These results indicate that the effect of ^{18}F adhesion to the PTFE tube lining is minimal during the various counting conditions during the length of the experiment, and the response of the ABSS is stable. However, this experiment should be repeated for other radioligands which could experience more stickiness to the PTFE. The determination of a constant calibration factor for the PBS-101 ABSS system aids in

minimizing the uncertainty of measurements and can eventually help eliminate the need for long acquisition times needed to capture accurate input function peaks for an individual.

The second sub-objective of Aim I characterized the response of the Hidex AMG, and the average efficiency and optimal range of activity were determined. Figure 5 (Section 3.2.2.2) depicts the average percent efficiency in both the 3.0 mL and 1.0 mL samples as a function of the logarithmic scale of activity (nCi), which indicated that the optimal range of activity of the AMG detector exists between 10-500 nCi. The results here provide information on the capacity of the AMG system for counting larger number of positron emission events, where at high concentrations of radioactivity the detector deadtime increases and therefore decreasing the overall counting efficiency.

From Figure 5, the average counting efficiency of ^{18}F for the 1.0 mL and 3.0 mL within the proposed optimal range of sensitivity of 10-500 nCi (Figure 6, Section 3.2.2.2) were determined to be 39.1±0.4% and 37.5±0.2% respectively. The results from the final experiment characterized the effect of sample volume on the average counting efficiency of measurements. As depicted in Figure 7 (Section 3.2.2.3) there is an observable decrease in the absolute counting efficiency of the AMG with increasing sample volume. This can be explained by the effect of the loss of counted emitted photons by the detector due to the geometry of positron emission (Figure 3, Section 2.6.3), resulting in more counts detected in the 511-keV peak ROI since there is less likelihood of capturing both photons in coincidence in the 1022-keV peak ROI. These results are consistent with the results of a similar study that characterized a commercial well-type NaI(TI) gamma counter for PET applications (Wizard^2, PerkinElmer, Waltham, MA, USA) [77]. Here, Martin A. Lodge *et al.* (2015) reported a similar effect, where the relative efficiencies centered

around the 511-keV photon peak were less susceptible to changes in sample volumes than those of single-photon emitters.

A similar experiment was conducted, instead to determine the average counting efficiency of ^{11}C as a function of increasing sample sizes that represent the volumes required for plasma metabolite analysis of [^{11}C]CURB. Again, there is an observed decrease in the counting efficiency of ^{11}C as sample volumes increase. In addition, the average percent efficiency of data measured within the counting window of energy used in the SOP for the metabolite analyses (400-600 keV) was compared to that of the average percent efficiency of data acquired in an energy window that is centered exactly ±20% of the 511-keV peak (409-613 keV). The efficiency for the 400-600 keV energy window and the 409-613 keV energy window were determined to be 32.7% and 33.0% respectively, which validates the accuracy of the window of energy used for the plasma metabolite analyses. The observation that the percent efficiency for ^{11}C is lower than that of ^{18}F is surprising since all data was corrected for the branching ratio of each radioisotope. Some possible explanations include the potential higher levels of adhesion of the tracer to the syringes used to transfer the solutions and any other elements used when diluting the solutions. In addition, the short half-life of ^{11}C makes it particularly more challenging to account for measurement error corrections.

6.2 Investigation into [^{11}C]CURB 2-TCM*i* Macroparameters

The second aim of the present study involved the investigation into the identifiability and reproducibility between the three macroparameters of [^{11}C]CURB 2-TCM*i*: K_i, k_3, and λk_3. The macroparameter k_3 could not be considered the ideal rate constant for quantifying [FAAH] due to the known significant correlation to k_2, therefore increasing the occurrence of bias in the estimations of k_3 and low identifiability in small ROIs [2]. On the other hand, while K_i has

excellent identifiability for brain FAAH [2] it present a nonlinear dependence on k_3 which decrease the sensitivity to detect changes in [FAAH]. The composite parameter λk_3 was considered to be the recommended index for the PET quantification for FAAH activity in the brain as it has shown adequate identifiability, it is independent of rCBF, and because it is directly proportional to k_3, the irreversible trapping rate constant [2, 38]. The composition of λk_3 is such that it is independent of cerebral blood flow because contains the ratio K_1/k_2 and reduces the correlation between k_3 and k_2 because it contains the ratio k_3/k_2 [2, 78]. The results in this thesis, together with the reproducibility study performed by Isabelle Boileau *et al.* [38] suggest that for large cortical ROIs, k_3 is a potential alternative to quantify FAAH levels. Its correlation with k_2 does not affect its predictability of the genotype effect in the FAAH level. The validity of the results should be confirmed with larger sample sizes. Therefore, in Aim II of the present study, the main goal was to expand on these validation studies using larger samples sizes of healthy volunteers as well as assessing the optimum parameter for quantifying FAAH in the brain based on the size of the ROI.

In PET neuroimaging, the size of the ROI influences the level of noise and variance in parameter to quantify the radioligand. The more counts captured from an ROI will produce more uniform images and less variability, therefore improving the reproducibility of measurements [79, 80]. In small ROIs, there will be fewer positron emission events captured by the PET detector [79]. Therefore, the measurements acquired will have higher levels of noise and variability, decreasing the statistical power of repeatability of the estimated model parameters. In larger ROIs, the influence of noise is not as significant, making the measurements more reliable and less variable. Therefore, to evaluate the identifiability and sensitivity between the

[^{11}C]CURB 2-TCM*i* macroparameters, the values estimated by each in the temporal cortex (as the large ROI) were compared to the values of the dorsal caudate nucleus (as the small ROI).

It was hypothesized that in a larger ROI k_3 will have the highest sensitivity for detecting changes in FAAH binding between C/C and A/C rs324420 SNPs, and conversely λk_3 would have the highest sensitivity in small ROIs. The rationale behinds these hypotheses are based on the levels of noise between the ROIs, where in the temporal cortex the estimated parameters will have less variability and uncertainty compared to the large level of uncertainty when using a small ROI such as the dorsal caudate. 2-TCM*i* k_3 and k_2 are known to strongly correlate for [^{11}C]CURB due to noise and insufficiencies of the model, therefore the values provided by the 2-TCM*i* present low identifiability (high associated error) for their individual estimations. It was predicted λk_3 would be a more stable measure to quantify [FAAH] since it incorporated the ratio k_3/k_2 in its calculations, therefore canceling out the error related to the correlation. However, on the other hand, λ has information about the free and non-specific binding which is a source of variability between subjects when we try to quantify FAAH. The results from the temporal cortex support the hypothesis that k_3 (P=4.18e10^{-5}) has the highest sensitivity for detecting changes in [FAAH]. Furthermore, the results from the dorsal caudate support the hypothesis that λk_3 (P=0.002) has the greatest sensitivity for detecting changes in [FAAH]. The Monte Carlo simulations predicts reasonable samples sizes to observe differences using λk_3 in the dorsal caudate (n = 10, 8, 4, for 15%, 20% and 25% reductions in [FAAH] respectively). In summary, these results indicate that all three parameters are appropriate measures for indexing [FAAH] in the brain but depending on the level of noise within a specified ROI the effect size measure for each parameter will be different. The best index for detecting changes is dependent on the specified ROI.

6.3 Averaged Metabolization Peak Input Function

There are several proposed approaches for estimating the arterial input function and metabolization of a radiotracer in tissue, all with varying levels of uncertainty and limitations. It is well established that the only standard approached for estimating the AIF is through arterial blood sampling in combination with plasma metabolite analyses [5, 42]. While arterial blood sampling is considered a robust and accurate measure of the true delivery function of parent radiotracer in arterial plasma, it is an experimentally challenging and laborious approach [6]. Therefore, there remains a demand for facilitating less invasive and increasingly automated techniques in image analysis to promote the engagement of study participants and improve the reliability of analysis methods. Accurate radiometabolite correction improves the estimation of the kinetic parameters used in the modeling of radiotracer uptake and metabolism. This correction can have a significant impact on the quantification of receptor binding, enhancing the reliability of PET imaging results.

In Aim III of the present study, the goal was to develop a computational estimation of the plasma metabolization correct input function to not only reduce the potential complications during arterial blood sampling, but to also assess the level of detail required to accurately estimate parameters in [^{11}]CURB compartmental modeling. This approach used an averaged value of both the whole-blood and metabolite-corrected plasma activity curves during the crucial first 15 minutes post bolus injection, where the changes in availability of radioligand are the most rapid. The normalized PAPs to the biexponential of the manual samples were used to determine individual APIF and APWBs for each subject. The individually normalized APIF and APWBs were then used in the computation and re-estimation of the macroparameter λk_3 of the [^{11}C]CURB 2-TCM*i*. The sensitivity of the APIF method for detecting the changes in [FAAH]

between C/C and A/C genotypes compared to the gold-standard AIF method (Figure 20, Section 5.2) supported the hypothesis that this simplified approach would be successful in accurately reproducing the polymorphism effect with no apparent bias (Figures 17-19). Although, this approach appears to not have enough sensitivity to small changes and it would require larger sample sizes, in comparison to AIF, which eventually could not be feasible to recruit in a real clinical experiment.

The results of Aim III taken provide support that applying the APIF modeling approach does not produce any significant biases and had acceptable ranges of uncertainty. The results indicate that this method would be an appropriate approach to still be able to correct data for metabolization to compute the accurate kinetic modeling when the ABSS data is lost due to experimental error. Although, the primary limitation of this method is by using an averaged IF value, the capture of individual rapid changes is lost, and it reduces sensitivity and will require larger sample sizes to obtain significance. In conclusion, the evidence from this study indicates that quantifying individual measurements of radioligand metabolization is crucial for the statistical power, identifiability, and sensitivity for modeling the kinetics of PET radiotracers.

7. Conclusion and Expected Contribution to Original Knowledge

The present study provides the technical performance, characterization, and stability of required instrumentation for radioligand quantification in arterial blood sampling. It also offers novel investigations into the sensitivity and reliability of varying computational approaches to modeling FAAH binding in the brain using [^{11}C]CURB PET imaging. It also presents a novel investigation into the sensitivity of the outcome parameters of the 2-TCMi (K_i, λk_3 and k_3) to quantify [^{11}C]CURB PET imaging and an estimation of the increase of variability in [^{11}C]CURB λk_3 when the ABSS measurement is not available, and it is replaced by an average measurement based on other subjects.

Gamma counters are necessary for the radioligand quantification in arterial blood for in-vivo PET imaging quantification using full kinetic modeling. The proper calibration and characterization of the response of the required instrumentation has an important role in the accuracy and reproducibility of the clinical applications [12, 65]. Here, we report the comprehensive characterization and calibration of a full programmable ABSS system and an automated gamma counter (AMG).

In addition, we report the strengths and drawbacks of the available arterial sampling techniques and offer a computational alternative to simplify the protocol for extraction of arterial blood. Our aim was to assess the importance of individualized arterial sampling. While acquiring individual AIFs for each participant produces more precise estimation of 2-TCM*i* macroparameters, using the APIF is a reliable method with limited bias and variability introduced to parameter estimations.

8. References

[1] Garani R, Watts JJ, Mizrahi R. Endocannabinoid system in psychotic and mood disorders, a review of human studies. Progress in Neuro-Psychopharmacology and Biological Psychiatry. 2021;106:110096. doi:10.1016/j.pnpbp.2020.110096

[2] Rusjan PM, Wilson AA, Mizrahi R, Boileau I, Chavez SE, Lobaugh NJ, Kish SJ, Houle S, Tong J. Mapping Human Brain Fatty Acid Amide Hydrolase Activity with PET. Journal of Cerebral Blood Flow & Metabolism. 2013;33(3):407–414. doi:10.1038/jcbfm.2012.180

[3] Carson RE. 6 Tracer Kinetic Modeling in PET. Positron Emission Tomography: Basic Science and Clinical Practice. 2003:147–179.

[4] Ghosh KK, Padmanabhan P, Yang C-T, Mishra S, Halldin C, Gulyás B. Dealing with PET radiometabolites. EJNMMI Research. 2020;10:109. doi:10.1186/s13550-020-00692-4

[5] Tonietto M, Rizzo G, Veronese M, Fujita M, Zoghbi SS, Zanotti-Fregonara P, Bertoldo A. Plasma radiometabolite correction in dynamic PET studies: Insights on the available modeling approaches. Journal of Cerebral Blood Flow & Metabolism. 2016;36(2):326–339. doi:10.1177/0271678X15610585

[6] Jons PH, Ernst M, Hankerson J, Hardy K, Zametkin AJ. Follow-up of radial arterial catheterization for positron emission tomography studies. Human Brain Mapping. 1997;5(2):119–123. doi:10.1002/(SICI)1097-0193(1997)5:2<119::AID-HBM5>3.0.CO;2-6

[7] Gunn R. Mathematical Modelling and Identifiability Applied to Positron Emission Tomography Data. 1996:227.

[8] Nakao R, Schou M, Halldin C. Rapid metabolite analysis of positron emission tomography radioligands by direct plasma injection combining micellar cleanup with high submicellar liquid chromatography with radiometric detection. Journal of Chromatography A. 2012;1266:76–83. doi:10.1016/j.chroma.2012.10.022

[9] Katsifis A, Loc'h C, Henderson D, Bourdier T, Pham T, Greguric I, Lam P, Callaghan P, Mattner F, Eberl S, et al. A rapid solid-phase extraction method for measurement of non-metabolised peripheral benzodiazepine receptor ligands, [(18)F]PBR102 and [(18)F]PBR111, in rat and primate plasma. Nuclear Medicine and Biology. 2011;38(1):137–148. doi:10.1016/j.nucmedbio.2010.07.008

[10] Boellaard R, van Lingen A, van Balen SCM, Hoving BG, Lammertsma AA. Characteristics of a new fully programmable blood sampling device for monitoring blood radioactivity during PET. European Journal of Nuclear Medicine. 2001;28(1):81–89. doi:10.1007/s002590000405

[11] Programmable Blood Sampler (PBS-101-UM-01-EN): Use and maintenance manual. 2014.

[12] Lodge MA, Holt DP, Kinahan PE, Wong DF, Wahl RL. Performance assessment of a NaI(Tl) gamma counter for PET applications with methods for improved quantitative accuracy and greater standardization. EJNMMI Physics. 2015;2:11. doi:10.1186/s40658-015-0114-3

[13] Haaf FELT, Verheijke ML. An improved gamma well counter for radioactive tracer applications. The International Journal of Applied Radiation and Isotopes. 1976;27(2):79–84. doi:10.1016/0020-708X(76)90180-0

[14] Gunn RN, Gunn SR, Cunningham VJ. Positron Emission Tomography Compartmental Models. Journal of Cerebral Blood Flow & Metabolism. 2001;21(6):635–652. doi:10.1097/00004647-200106000-00002

[15] Daghighian F, Sumida R, Phelps ME. PET Imaging: An Overview and Instrumentation. Journal of Nuclear Medicine Technology. 1990;18(1):5–13.

[16] Townsend D. Physical Principles and Technology of Clinical PET Imaging. 2004;33(2).

[17] Zhu Y, Zhu X. MRI-Driven PET Image Optimization for Neurological Applications. Frontiers in Neuroscience. 2019;13:782. doi:10.3389/fnins.2019.00782

[18] Chen Y, An H. Attenuation Correction of PET/MR Imaging. Magnetic resonance imaging clinics of North America. 2017;25(2):245–255. doi:10.1016/j.mric.2016.12.001

[19] Rusjan P, Mamo D, Ginovart N, Hussey D, Vitcu I, Yasuno F, Tetsuya S, Houle S, Kapur S. An automated method for the extraction of regional data from PET images. Psychiatry Research: Neuroimaging. 2006;147(1):79–89. doi:10.1016/j.pscychresns.2006.01.011

[21] Morris ED, Endres CJ, Schmidt KC, Christian BT, Jr RFM, Fisher RE. Kinetic Modeling in Positron Emission Tomography.

[22] Innis RB, Cunningham VJ, Delforge J, Fujita M, Gjedde A, Gunn RN, Holden J, Houle S, Huang S-C, Ichise M, et al. Consensus Nomenclature for in vivo Imaging of Reversibly Binding Radioligands. Journal of Cerebral Blood Flow & Metabolism. 2007;27(9):1533–1539. doi:10.1038/sj.jcbfm.9600493

[23] Wilson AA, Garcia A, Parkes J, Houle S, Tong J, Vasdev N. [11C]CURB: Evaluation of a novel radiotracer for imaging fatty acid amide hydrolase by positron emission tomography. Nuclear Medicine and Biology. 2011;38(2):247–253. doi:10.1016/j.nucmedbio.2010.08.001

[24] Rusjan PM, Wilson AA, Mizrahi R, Boileau I, Chavez SE, Lobaugh NJ, Kish SJ, Houle S, Tong J. Mapping Human Brain Fatty Acid Amide Hydrolase Activity with PET. Journal of Cerebral Blood Flow & Metabolism. 2013;33(3):407–414. doi:10.1038/jcbfm.2012.180

[25] Palermo G, Branduardi D, Masetti M, Lodola A, Mor M, Piomelli D, Cavalli A, De Vivo M. Covalent inhibitors of fatty acid amide hydrolase (FAAH): A rationale for the activity of piperidine and piperazine aryl ureas. Journal of medicinal chemistry. 2011;54(19):6612–6623. doi:10.1021/jm2004283

[26] Ahn K, McKinney MK, Cravatt BF. Enzymatic Pathways That Regulate Endocannabinoid Signaling in the Nervous System. Chemical Reviews. 2008;108(5):1687–1707. doi:10.1021/cr0782067

[27] Skaper SD, Di Marzo V. Endocannabinoids in nervous system health and disease: the big picture in a nutshell. Philosophical Transactions of the Royal Society B: Biological Sciences. 2012;367(1607):3193–3200. doi:10.1098/rstb.2012.0313

[28] Pertwee RG, Howlett AC, Abood ME, Alexander SPH, Di Marzo V, Elphick MR, Greasley PJ, Hansen HS, Kunos G, Mackie K, et al. International Union of Basic and Clinical Pharmacology. LXXIX. Cannabinoid Receptors and Their Ligands: Beyond CB $_1$ and CB $_2$. Pharmacological Reviews. 2010;62(4):588–631. doi:10.1124/pr.110.003004

[29] Van Sickle MD, Duncan M, Kingsley PJ, Mouihate A, Urbani P, Mackie K, Stella N, Makriyannis A, Piomelli D, Davison JS, et al. Identification and Functional Characterization of Brainstem Cannabinoid CB2 Receptors. Science. 2005;310(5746):329–332. doi:10.1126/science.1115740

[30] Pertwee RG, Ross RA. Cannabinoid receptors and their ligands. Prostaglandins, Leukotrienes and Essential Fatty Acids (PLEFA). 2002;66(2–3):101–121. doi:10.1054/plef.2001.0341

[31] McKinney MK, Cravatt BF. Structure and Function of Fatty Acid Amide Hydrolase. Annual Review of Biochemistry. 2005;74(1):411–432. doi:10.1146/annurev.biochem.74.082803.133450

[32] Activation of the endocannabinoid system by organophosphorus nerve agents - PMC. [accessed 2023 Feb 10]. https://www-ncbi-nlm-nih-gov.proxy3.library.mcgill.ca/pmc/articles/PMC2597283/

[33] Hillard CJ. The Endocannabinoid Signaling System in the CNS. In: International Review of Neurobiology. Vol. 125. Elsevier; 2015. p. 1–47. https://linkinghub.elsevier.com/retrieve/pii/S0074774215001324. doi:10.1016/bs.irn.2015.10.001

[34] Jacobson MR, Watts JJ, Da Silva T, Tyndale RF, Rusjan PM, Houle S, Wilson AA, Ross RA, Boileau I, Mizrahi R. Fatty Acid Amide Hydrolase is Lower in Young Cannabis Users. Addiction biology. 2021;26(1):e12872. doi:10.1111/adb.12872

[35] Watts JJ, Jacobson MR, Lalang N, Boileau I, Tyndale RF, Kiang M, Ross RA, Houle S, Wilson AA, Rusjan P, et al. Imaging brain fatty acid amide hydrolase in untreated patients with psychosis. Biological psychiatry. 2020;88(9):727–735. doi:10.1016/j.biopsych.2020.03.003

[36] Lorthois S, Duru P, Billanou I, Quintard M, Celsis P. Kinetic modeling in the context of cerebral blood flow quantification by H2(15)O positron emission tomography: the meaning of the permeability coefficient in Renkin-Crone′s model revisited at capillary scale. Journal of Theoretical Biology. 2014;353:157–169. doi:10.1016/j.jtbi.2014.03.004

[37] Arakawa R, Takano A, Nag S, Jia Z, Amini N, Maresca KP, Zhang L, Keliher EJ, Butler CR, Piro JR, et al. Target occupancy study and whole-body dosimetry with a MAGL PET ligand [11C]PF-06809247 in non-human primates. EJNMMI Research. 2022;12(1):13. doi:10.1186/s13550-022-00882-2

[38] Boileau I, Rusjan PM, Williams B, Mansouri E, Mizrahi R, Luca VD, Johnson DS, Wilson AA, Houle S, Kish SJ, et al. Blocking of Fatty Acid Amide Hydrolase Activity with PF-04457845 in Human Brain: A Positron Emission Tomography Study with the Novel Radioligand [11C]CURB. Journal of Cerebral Blood Flow & Metabolism. 2015;35(11):1827–1835. doi:10.1038/jcbfm.2015.133

[39] Logan J, Fowler JS, Volkow ND, Wang G-J, MacGregor RR, Shea C. Reproducibility of repeated measures of deuterium substituted [11C]L-deprenyl ([11C]L-deprenyl-D2) binding in the human brain. Nuclear Medicine and Biology. 2000;27(1):43–49. doi:10.1016/S0969-8051(99)00088-8

[40] Pike VW. PET Radiotracers: crossing the blood-brain barrier and surviving metabolism. Trends in pharmacological sciences. 2009;30(8):431. doi:10.1016/j.tips.2009.05.005

[41] Aarnio R, Alzghool OM, Wahlroos S, O'Brien-Brown J, Kassiou M, Solin O, Rinne JO, Forsback S, Haaparanta-Solin M. Novel plasma protein binding analysis method for a PET tracer and its radiometabolites: A case study with [11C]SMW139 to explain the high uptake of radiometabolites in mouse brain. Journal of Pharmaceutical and Biomedical Analysis. 2022;219:114860. doi:10.1016/j.jpba.2022.114860

[42] Bentourkia M. Determination of the Input Function at the Entry of the Tissue of Interest and Its Impact on PET Kinetic Modeling Parameters. Molecular Imaging and Biology. 2015;17(6):748–756. doi:10.1007/s11307-015-0895-8

[43] Graham MM, Lewellen BL. High-Speed Automated Discrete Blood Sampling for Positron Emission Tomography.

[44] van der Weijden CWJ, Mossel P, Bartels AL, Dierckx RAJO, Luurtsema G, Lammertsma AA, Willemsen ATM, de Vries EFJ. Non-invasive kinetic modelling approaches for quantitative analysis of brain PET studies. European Journal of Nuclear Medicine and Molecular Imaging. 2023;50(6):1636–1650. doi:10.1007/s00259-022-06057-4

[45] Gumbleton M, Oie S, Verotta D. Pharmacokinetic-pharmacodynamic (PK-PD) modelling in non-steady-state studies and arterio-venous drug concentration differences. British Journal of Clinical Pharmacology. 1994;38(5):389–400. doi:10.1111/j.1365-2125.1994.tb04372.x

[46] Tomasi G, Veronese M, Bertoldo A, Smith CB, Schmidt KC. Substitution of venous for arterial blood sampling in the determination of regional rates of cerebral protein synthesis with L-[1-11C]leucine PET: A validation study. Journal of Cerebral Blood Flow & Metabolism. 2019;39(9):1849–1863. doi:10.1177/0271678X18771242

[47] Green JH, Ellis FR, Shallcross TM, Bramley PN. Invalidity of hand heating as a method to arterialize venous blood. Clinical Chemistry. 1990;36(5):719–722.

[48] Chiou WL. The Phenomenon and Rationale of Marked Dependence of Drug Concentration on Blood Sampling Site. Clinical Pharmacokinetics. 1989;17(3):175–199. doi:10.2165/00003088-198917030-00004

[49] Zanotti-Fregonara P, Chen K, Liow J-S, Fujita M, Innis RB. Image-derived input function for brain PET studies: many challenges and few opportunities. Journal of Cerebral Blood Flow & Metabolism. 2011;31(10):1986–1998. doi:10.1038/jcbfm.2011.107

[50] Bartlett EA, Ananth M, Rossano S, Zhang M, Yang J, Lin S, Nabulsi N, Huang Y, Zanderigo F, Parsey RV, et al. Quantification of Positron Emission Tomography Data Using Simultaneous Estimation of the Input Function: Validation with Venous Blood and Replication of Clinical Studies. Molecular Imaging and Biology. 2019;21(5):926–934. doi:10.1007/s11307-018-1300-1

[51] Brooks DC, Black PR, Arcangeli MA, Aoki TT, Wilmore DW. The Heated Dorsal Hand Vein: An Alternative Arterial Sampling Site. Journal of Parenteral and Enteral Nutrition. 1989;13(1):102–105. doi:10.1177/0148607189013001102

[52] Zanotti-Fregonara P, Hines CS, Zoghbi SS, Liow J-S, Zhang Y, Pike VW, Drevets WC, Mallinger AG, Zarate CA, Fujita M, et al. Population-based input function and image-derived input function for [11C](R)-rolipram PET imaging: Methodology, validation and application to the study of major depressive disorder. NeuroImage. 2012;63(3):1532–1541. doi:10.1016/j.neuroimage.2012.08.007

[53] Mabrouk R, Strafella AP, Knezevic D, Ghadery C, Mizrahi R, Gharehgazlou A, Koshimori Y, Houle S, Rusjan P. Feasibility study of TSPO quantification with [18F]FEPPA using population-based input function. PLOS ONE. 2017;12(5):e0177785. doi:10.1371/journal.pone.0177785

[54] Rissanen E, Tuisku J, Luoto P, Arponen E, Johansson J, Oikonen V, Parkkola R, Airas L, Rinne JO. Automated reference region extraction and population-based input function for brain [11C]TMSX PET image analyses. Journal of Cerebral Blood Flow and Metabolism. 2015;35(1):157–165. doi:10.1038/jcbfm.2014.194

[55] Takikawa S, Dhawan V, Chaly T, Robeson W, Dahl R, Zanzi I, Mandel F, Spetsieris P, Eidelberg D. Input Functions for 6-[Fluorine-18]Fluorodopa Quantitation in Parkinsonism: Comparative Studies and Clinical Correlations. Journal of Nuclear Medicine. 1994;35(6):955–963.

[56] Zanotti-Fregonara P, Liow J-S, Fujita M, Dusch E, Zoghbi SS, Luong E, Boellaard R, Pike VW, Comtat C, Innis RB. Image-Derived Input Function for Human Brain Using High Resolution PET Imaging with [11C](R)-rolipram and [11C]PBR28 Gelovani J, editor. PLoS ONE. 2011;6(2):e17056. doi:10.1371/journal.pone.0017056

[57] Meechai T, Tepmongkol S, Pluempitiwiriyawej C. Partial-volume effect correction in positron emission tomography brain scan image using super-resolution image reconstruction. The British Journal of Radiology. 2015;88(1046):20140119. doi:10.1259/bjr.20140119

[58] Chen K, Bandy D, Reiman E, Huang SC, Lawson M, Feng D, Yun LS, Palant A. Noninvasive quantification of the cerebral metabolic rate for glucose using positron emission tomography, 18F-fluoro-2-deoxyglucose, the Patlak method, and an image-derived input function. Journal of Cerebral Blood Flow and Metabolism: Official Journal of the International Society of Cerebral Blood Flow and Metabolism. 1998;18(7):716–723. doi:10.1097/00004647-199807000-00002

[59] Lammertsma AA, Hume SP. Simplified Reference Tissue Model for PET Receptor Studies. NeuroImage. 1996;4(3):153–158. doi:10.1006/nimg.1996.0066

[60] Litton J-E, Hall H, Pauli S. Saturation Analysis in PET—Analysis of Errors Due to Imperfect Reference Regions. Journal of Cerebral Blood Flow & Metabolism. 1994;14(2):358–361. doi:10.1038/jcbfm.1994.45

[61] Compartmental Analysis of Diprenorphine Binding to Opiate Receptors in the Rat in vivo and its Comparison with Equilibrium Data in vitro - Vincent J. Cunningham, Susan P. Hume, Gary R. Price, Randall G. Ahier, Jill E. Cremer, Anthony K. P. Jones, 1991. [accessed 2023 Jun 11]. https://journals-sagepub-com.proxy3.library.mcgill.ca/doi/10.1038/jcbfm.1991.1

[62] Guo Q, Owen DR, Rabiner EA, Turkheimer FE, Gunn RN. A graphical method to compare the in vivo binding potential of PET radioligands in the absence of a reference region: application to [11C]PBR28 and [18F]PBR111 for TSPO imaging. Journal of Cerebral Blood Flow & Metabolism. 2014;34(7):1162–1168. doi:10.1038/jcbfm.2014.65

[63] Logan J, Fowler JS, Volkow ND, Wang GJ, Ding YS, Alexoff DL. Distribution volume ratios without blood sampling from graphical analysis of PET data. Journal of Cerebral Blood Flow and Metabolism: Official Journal of the International Society of Cerebral Blood Flow and Metabolism. 1996;16(5):834–840. doi:10.1097/00004647-199609000-00008

[64] Lodge MA, Holt DP, Kinahan PE, Wong DF, Wahl RL. Performance assessment of a NaI(Tl) gamma counter for PET applications with methods for improved quantitative accuracy and greater standardization. EJNMMI Physics. 2015;2(1):11. doi:10.1186/s40658-015-0114-3

[65] Zanzonico P. Routine Quality Control of Clinical Nuclear Medicine Instrumentation: A Brief Review. Journal of nuclear medicine : official publication, Society of Nuclear Medicine. 2008;49(7):1114–1131. doi:10.2967/jnumed.107.050203

[66] Boileau I, Tyndale RF, Williams B, Mansouri E, Westwood DJ, Foll BL, Rusjan PM, Mizrahi R, De Luca V, Zhou Q, et al. The Fatty Acid Amide Hydrolase C385A Variant Affects Brain Binding of the Positron Emission Tomography Tracer [11C]CURB. Journal of Cerebral Blood Flow & Metabolism. 2015;35(8):1237–1240. doi:10.1038/jcbfm.2015.119

[67] Sipe JC, Chiang K, Gerber AL, Beutler E, Cravatt BF. A missense mutation in human fatty acid amide hydrolase associated with problem drug use. Proceedings of the National Academy of Sciences of the United States of America. 2002;99(12):8394–8399. doi:10.1073/pnas.082235799

[68] Rusjan P, Mamo D, Ginovart N, Hussey D, Vitcu I, Yasuno F, Tetsuya S, Houle S, Kapur S. An automated method for the extraction of regional data from PET images. Psychiatry Research: Neuroimaging. 2006;147(1):79–89. doi:10.1016/j.pscychresns.2006.01.011

[69] Tu Z, Mach RH. C-11 radiochemistry in cancer imaging applications. Current Topics in Medicinal Chemistry. 2010;10(11):1060–1095. doi:10.2174/156802610791384261

[70] Hidex Automatic Gamma Counter - User Guide, Version 1.8. 2020. https://hidex.com/products/hidex-automatic-gamma-counter/

[71] Boileau I, Mansouri E, Williams B, Le Foll B, Rusjan P, Mizrahi R, Tyndale RF, Huestis MA, Payer DE, Wilson AA, et al. Fatty Acid Amide Hydrolase Binding in Brain of Cannabis Users: Imaging with the Novel Radiotracer [11C]CURB. Biological psychiatry. 2016;80(9):691–701. doi:10.1016/j.biopsych.2016.04.012

[72] Best LM, Hendershot CS, Buckman JF, Jagasar S, McPhee MD, Muzumdar N, Tyndale RF, Houle S, Logan R, Sanches M, et al. Association Between Fatty Acid Amide Hydrolase and Alcohol Response Phenotypes: A Positron Emission Tomography Imaging Study With [11C]CURB in Heavy-Drinking Youth. Biological Psychiatry. 2022 Dec:S0006322322018042. doi:10.1016/j.biopsych.2022.11.022

[75] Doğan NÖ. Bland-Altman analysis: A paradigm to understand correlation and agreement. Turkish Journal of Emergency Medicine. 2018;18(4):139–141. doi:10.1016/j.tjem.2018.09.001

[76] Pain F, Laniece P, Mastrippolito R, Gervais P, Hantraye P, Besret L. Arterial Input Function Measurement Without Blood Sampling Using a ᴺL-Microprobe in Rats.

[77] Lodge MA, Holt DP, Kinahan PE, Wong DF, Wahl RL. Performance assessment of a NaI(Tl) gamma counter for PET applications with methods for improved quantitative accuracy and greater standardization. EJNMMI Physics. 2015;2(1):11. doi:10.1186/s40658-015-0114-3

[78] Fowler JS, Logan J, Wang G-J, Volkow ND, Telang F, Ding Y-S, Shea C, Garza V, Xu Y, Li Z, et al. Comparison of the binding of the irreversible monoamine oxidase tracers, [11C]clorgyline and [11C]l-deprenyl in brain and peripheral organs in humans. Nuclear Medicine and Biology. 2004;31(3):313–319. doi:10.1016/j.nucmedbio.2003.10.003

[79] Jafari-Khouzani K, Paynabar K, Hajighasemi F, Rosen B. The effect of region of interest size on the repeatability of quantitative brain imaging biomarkers. IEEE transactions on bio-medical engineering. 2019;66(3):864–872. doi:10.1109/TBME.2018.2860928

[80] Hasford F, Wyk BV, Mabhengu T, Vangu MDT, Kyere AK, Amuasi JH. Effect of Radionuclide Activity Concentration on PET-CT Image Uniformity. World Journal of Nuclear Medicine. 2016;15(2):91–95. doi:10.4103/1450-1147.167578

9. Appendices

Appendix I *Supplemental Data*
Appendix I.a *Python Syntax for APIF*

New Plasma APIF:

```
import re
import math
from datetime import datetime


#You could also pass datetime.time object in this part and convert it to string.
time_scanner = str('hh:mm:ss')
time_inj = str('hh:mm:ss')

weight=## #kg
activity=## #mCi
SUV_factor=(activity*(10**6))/(weight*(10**3))     #nCi/ml  at time_of_injection.


coef_a=###
coef_b=###
coef_c=###
coef_d=###

biexpo = [(coef_a*math.exp(coef_b*t)+coef_c*math.exp(coef_d*t)) for t in
range(900, 62*60)]


# Then get the difference here.
diff = datetime.strptime(time_inj, "%H:%M:%S") - datetime.strptime(time_scanner,
"%H:%M:%S")
t_of_injection = diff.seconds
dcf=math.exp(math.log(2)*t_of_injection/1223.4)

biexpodcf=[e*dcf for e in biexpo]

print(dcf)
print(SUV_factor)


popif_times=[]
popif_act=[]
popif_actdcf=[]
```

```
with open('APIF_plasma_new.txt') as f:
    line = f.readline()
    line = f.readline()
    while line:
        popif=re.match('(\d+)\t[-+]?(\d+(\.\d*)?|\.\d+)',line)
        line = popif_times.append(popif.group(1))
        line = (popif_act.append(float(popif.group(2))*SUV_factor))
        line = popif_actdcf.append(float(popif.group(2))*SUV_factor*dcf)
        #print(act.group(2))
        line = f.readline()

#for t in popif_times:
#  print(t)

print(popif_times[10])


#estimate scale factor on t_inj
scale_factor=biexpo[0]/popif_act[900]
print(scale_factor)
print(SUV_factor)
exit()
#apply scale factor a popif

#recalculate the time with the delay of t_of_injection

time_sec = [t for t in range(0, 62*60+t_of_injection)]

input_function=[0 for t in range(0, t_of_injection)]
print(len(input_function))
print(input_function[len(input_function)-1])

xxx=[float(popif_actdcf[t])*scale_factor for t in range(0,900)]
input_function.extend(xxx)
input_function.extend(biexpodcf)



print(len(time_sec))
print(len(input_function))

#replace rescaled popbif

#save outpout
with open('CURB###_output_plasma_APIF_new.smpl', 'w') as f:
```

```
    f.write("Time[seconds]\tPlasma[nCi/cc]\n")
    for item in time_sec:
        f.write( str(item) + "\t" + str( input_function[item] ) + "\n" )
```

New Whole-Blood APIF:

```
import re
import math
from datetime import datetime


#You could also pass datetime.time object in this part and convert it to string.
time_scanner = str('hh:mm:ss')
time_inj = str('hh:mm:ss')

weight=##  #kg
activity=##   #mCi
SUV_factor=(activity*(10**6))/(weight*(10**3))     #nCi/ml  at time_of_injection.


coef_a=###
coef_b=###
coef_c=###
coef_d=###

biexpo = [(coef_a*math.exp(coef_b*t)+coef_c*math.exp(coef_d*t)) for t in
range(900, 62*60)]


# Then get the difference here.
diff = datetime.strptime(time_inj, "%H:%M:%S") - datetime.strptime(time_scanner,
"%H:%M:%S")
t_of_injection = diff.seconds
dcf=math.exp(math.log(2)*t_of_injection/1223.4)

biexpodcf=[e*dcf for e in biexpo]

print(dcf)
print(SUV_factor)


popif_times=[]
popif_act=[]
popif_actdcf=[]
```

```
with open('APIF_WBlood_new.txt') as f:
    line = f.readline()
    line = f.readline()
    while line:
        popif=re.match('(\d+)\t[-+]?(\d+(\.\d*)?|\.\d+)',line)
        line = popif_times.append(popif.group(1))
        line = (popif_act.append(float(popif.group(2))*SUV_factor))
        line = popif_actdcf.append(float(popif.group(2))*SUV_factor*dcf)
        #print(act.group(2))
        line = f.readline()

#for t in popif_times:
#  print(t)

print(popif_times[10])


#estimate scale factor on t_inj
scale_factor=biexpo[0]/popif_act[900]
print(scale_factor)
print(SUV_factor)
exit()
#apply scale factor a popif

#recalculate the time with the delay of t_of_injection

time_sec = [t for t in range(0, 60*62+t_of_injection)]

input_function=[0 for t in range(0, t_of_injection)]
print(len(input_function))
print(input_function[len(input_function)-1])

xxx=[float(popif_actdcf[t])*scale_factor for t in range(0,900)]
input_function.extend(xxx)
input_function.extend(biexpodcf)



print(len(time_sec))
print(len(input_function))

#replace rescaled popbif

#save outpout
with open('CURB###_new_output_WB_APIF.smpl', 'w') as f:
```

```
    f.write("Time[seconds]\tBlood[nCi/cc]\n")
    for item in time_sec:
        f.write( str(item) + "\t" + str( input_function[item] ) + "\n" )
```

Appendix I.b *MATLAB Syntax for Monte Carlo Simulations*

```
clear all


no_sim=2000;
max_n=100;

% reduction = 0.10
% reduction=0.15
% reduction=0.20
% reduction=0.25

for n=2:max_n    %SAMPLE SIZE SUGGESTED
    for i=1:no_sim  %NUMBER OF SIMULATION
clear group
clear snp
   % n=10
hv_cc = 0.18 + 0.034.*randn(n,1);    %GROUP 1 mean+SD, genotype CC
hv_ca= 0.15 + 0.019.*randn(n,1);    %GROUP 1 mean+SD, genotype CA
dc_cc= 0.18* (1-reduction) + 0.034.*randn(n,1); %GROUP 2 mean+SD, genotype CC
dc_ca= 0.15*(1-reduction) + 0.019.*randn(n,1); %GROUP 2 mean+SD, genotype CA
y=[hv_cc ; hv_ca ;dc_cc;  dc_ca];
group(1:n*2)=1;
group(2*n+1:n*4)=2;
snp(1:n)=1;
snp(n+1:n*2)=2;
snp(2*n+1:3*n)=1;
snp(3*n+1:n*4)=2;
%same result as SPSS general linear models, Univariate analysis, fix factors:
group and snp, no include intercept
 [p,tbl,stats,terms] = anovan(y,{group
snp},'model','interaction','varnames',{'group','snp'},'display' ,'off');
 P(i,n)=p(1);
 %[H,P(i,n),CI,STATS] =ttest(hc_cc,hc_ca);
end
end

 p=sum(P<0.05)/no_sim;
```

```
%PLOT
 pp = movmean(p,10)
 display('n per group:')
 k = find(pp>0.95,1)
 n=1:max_n;
 p095(n)=0.95;
plot(n,p,'r-',[k k],[0 1],'b-',n,p095,'g-')
```